Enhancing ion-electron transport in positive electrode of solid-state lithium metal batteries with multifunctional catholyte made of polymer mixed ionic-electronic conductor PEDOT:PSSTFSI and Li3InCl6

Elina Nazmutdinova, Ivone Marselina Nugraha, Jacob Olchowka, Eric Cloutet, Cyril Brochon, André Gröschel, Laurence Croguennec

To cite this version:

Elina Nazmutdinova, Ivone Marselina Nugraha, Jacob Olchowka, Eric Cloutet, Cyril Brochon, et al.. Enhancing ion-electron transport in positive electrode of solid-state lithium metal batteries with multifunctional catholyte made of polymer mixed ionic-electronic conductor PEDOT:PSSTFSI and Li3InCl6. Advanced Energy Materials, 2026, 16 (14), pp.e06757. ⟨10.1002/aenm.202506757⟩. ⟨hal-05538922⟩

HAL Id: hal-05538922
https://hal.science/hal-05538922v1

Submitted on 9 Mar 2026

Enhancing Ion-Electron Transport in Positive Electrode of Solid-State Lithium Metal Batteries with Multifunctional Catholyte Made of Polymer Mixed Ionic-Electronic Conductor PEDOT:PSSTFSI and Li_3InCl_6

Elina Nazmutdinova[#], Ivone Marselina Nugraha[#], Jacob Olchowka, Eric Cloutet, Cyril Brochon, André Gröschel, Laurence Croguennec**

[#] Elina Nazmutdinova and Ivone Marselina Nugraha contributed equally to this work.

I.M. Nugraha, J. Olchowka, L. Croguennec
Univ. Bordeaux, CNRS, Bordeaux INP, ICMCB, UMR 5026, F-33600 Pessac, France
I.M. Nugraha, J. Olchowka, L. Croguennec
RS2E, Réseau Français sur le Stockage Electrochimique de l'Energie, CNRS FR 3459, 80039 Amiens Cedex 1, France
I.M. Nugraha, J. Olchowka, L. Croguennec
ALISTORE-ERI, FR CNRS 3104 33 Rue Saint-Leu, 80039 Amiens Cedex 1, France
I.M. Nugraha, E. Cloutet. C. Brochon
Univ. Bordeaux, CNRS, Bordeaux INP, LCPO, UMR5629, Allée Geoffroy Saint Hilaire, Bâtiment B8, F-33607 Pessac, France
E. Nazmutdinova, A. Gröschel
Bavarian Center for Battery Technology (BayBatt), University of Bayreuth, Universitätsstrasse 30, 95447 Bayreuth, Germany
E-mail: laurence.croguennec@icmcb.cnrs.fr, andre.groeschel@uni-bayreuth.de

Funding: LC acknowledges Horizon 2020 research and innovation program under the Marie Skłodowska-Curie Actions (Grant Agreement No. 945357, Destiny PhD Program), the Nouvelle-Aquitaine Region (Project AAPR2021A-2020-11998810) and the French National Research Agency (STORE- EX Labex Project ANR- 10-LABX-76-01). AHG acknowledges funding through the Hightech Agenda Bavaria, BayFrance (Franco-Bavarian University Cooperation Center) and the German research foundation through project number 568901658.

Keywords: all solid-state batteries, composite materials, halide solid electrolytes, mixed ionic-electronic conductive polymers, positive electrodes.

Abstract

The development of positive electrode composites (PECs) with improved ionic and electronic conductivity is critical for high-performance all-solid-state batteries (ASSBs). Conventional strategies rely on tuning the ratio of positive active material (CAM) to solid electrolyte (SE) or introducing electronic conductive additives, yet both often induce interfacial instabilities limiting long-term performance. Here, mixed ionic-electronic conductor, poly(3,4-ethylenedioxythiophene): poly(4-styrenesulfonyl(trifluoromethylsulfonyl)imide) (PEDOT:PSSTFSI), is incorporated as a functional polymer (FP) binder in Li_3InCl_6 (LIC), forming multifunctional catholytes in a single step via one-pot aqueous synthesis. Owing to π-π stacking and $TFSI^-$ functional group, PEDOT:PSSTFSI enhances electronic and ionic conductivity within the catholyte. Compared to the polymer-free NMC-based PEC, incorporating 5 wt.% FP markedly increases electrode compactness, reducing the porosity by 41.8% and yielding a twelvefold increase in effective electronic conductivity. In parallel, ionic conductivity improves substantially – up to 15-fold, with the highest reached at 0.6 wt.% of FP in the PEC. When tested in ASSBs cells, PEC containing FP shows enhanced rate capability, especially at 1C rate with full reversibility, and delivers up to 30% higher discharge capacity at a C/20 rate compared to polymer-free NMC-LIC references. This study highlights mixed conducting binders as a versatile system to improve conducting pathways while enhancing electrode integrity.

Table of Contents

A mixed ion-electron conducting polymer binder, PEDOT:PSSTFSI, enhances both ionic and electronic transport in NMC-based positive electrode composite (PEC) for ASSBs. Optimal polymer loading (0.33 wt.% in PEC) provides the most balanced transport, with an effective conductivities ($\sigma_{el.}/\sigma_{ion.}$) ratio closest to unity, enabling high discharge capacity at 1C. Deviations from this balance reduce high-rate performance and shorten cell lifetime.

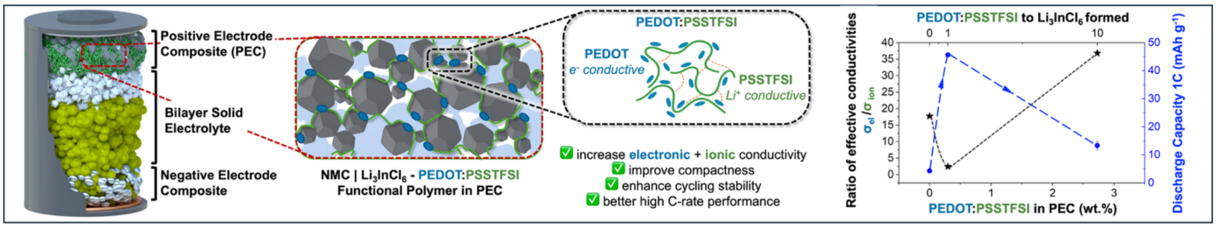

1. Introduction

With the rise in demand for batteries with higher energy density, along with improved safety and broad operating conditions, all solid-state batteries (ASSBs) have emerged as an appealing future-generation technology. By replacing the flammable liquid electrolyte used in conventional Li-ion batteries (LIBs) with solid electrolyte (SE), ASSBs enable safer use of Li metal as negative electrode together with high-voltage and high-capacity positive electrode materials.[1,2] While state-of-the-art LIBs approach their theoretical energy density ceiling of 300 Wh kg^{-1},[3,4] this design of ASSBs allows considerably higher energy densities up to 400 Wh kg^{-1} and beyond, while reducing the risks of thermal runaway.[2] ASSBs also offer an expanded range of operating temperatures, *i.e.* up to +150 °C[5] and as low as -60 °C.[6,7] Owing to the combination of high energy density and improved safety, ASSBs offer greater versatility and enable applications in electric vehicles and grid-scale energy storage.

Despite their numerous advantages, ASSBs still face several critical challenges that limit their performance. Given that these systems consist entirely of solid components, interfacial issues are particularly pronounced, especially within the multi-component positive electrode composite (PEC).[8,9] In ASSBs, the PEC primarily consists of the cathode active material (CAM) and a solid electrolyte (so-called catholyte), a significant fraction of which is required to ensure sufficient ionic conductivity in the absence of a pore-infiltrating liquid electrolyte.[10,11] Current positive electrodes in ASSB often contain up to 40 vol.% of catholyte, limiting the CAM content to less than 60 vol.%, compared to more than 85 vol.% in liquid systems.[12] Although high catholyte content provides ionic percolation, it reduces energy density by increasing the volume of inactive material and by disrupting electronic pathways.[13] This, in turn, often necessitates the addition of conductive additives, which further reduces the CAM content. Conventional electronic conductive additives such as carbon black, carbon nanotubes, and vapor-grown carbon fibers (VGCF) are commonly used to enhance electronic transport in ASSB positive electrodes[14–16], but they do not contribute to ionic conductivity. Moreover, some conductive carbons have been reported to catalyze parasitic reactions, such as oxidative decomposition of electrolyte on the carbon surface, producing reactive by-products further accelerating oxidation of CAM, ultimately leading to catholyte decomposition and accelerated capacity fading of the battery.[17]

Furthermore, ASSBs' PEC are solid-phase heterogeneous mixtures that frequently suffer from interparticle contact loss and poor interfacial connectivity, particularly when the CAM undergoes volumetric changes during cycling due to insertion and extraction of Li^{+} ions.[18,19] In

ASSBs, such repetitive volume changes cannot be easily accommodated, resulting in stress accumulation at the CAM-SE interface. This accumulated stress compromises the mechanical integrity of the PEC, leading to microstructural fracturing of both the SE and CAM, along with formation of interfacial cracks due to contact loss at the CAM-SE interfaces, ultimately disrupting the ion-electron transport networks within the PEC. Therefore, to improve interparticle contact and accommodate volumetric changes, ASSBs often require the application of high external pressure during operation, which complicates cell design and limits scalability.[20,21] Another approach to improve interparticle contact and adhesion is the incorporation of polymer binders.[22] However, commonly used binders such as polyvinylidene fluoride (PVDF), polytetrafluoroethylene (PTFE) or styrene-butadiene rubber (SBR), are intrinsically electronic and ionic insulating, which may hinder charge transport, decreasing overall electrode performance. Here, hybrid polymer/inorganic electrolytes provide key insights for positive electrode composites. In Li_3InCl_6-based solid-electrolytes hybrids, non-conductive polymers are bottlenecks for conduction, dominated by interfaces,[23] meanwhile addition of lithium bis(trifluoromethanesulfonyl)imide (LiTFSI) salt can help tune conductivity,[24] stressing out multi-component optimization. Reviews confirm the complexity of transport mechanisms through multi-component SE hybrids that can be partially applicable to more complex positive electrode composite systems.[25,26]

The numerous challenges highlight the need for multifunctional additives that not only improve electronic and ionic transport within the PEC but also provide a binding matrix to accommodate volumetric changes during cycling.[10,11] In contrast, incorporating additives with both ionic and electronic conductivity opens a pathway to reduce the deadweight by minimizing the content of non-active components while maintaining interfacial contact, thereby enabling higher CAM loadings and improved energy density. Therefore, developing functional polymeric materials that exhibit ionic conductivity[27,28], electronic conductivity[29,30], or even both[31,32] is a promising approach to address these issues.

Among such materials, PEDOT-based mixed ionic-electronic conductive polymers have emerged as promising multifunctional materials in ASSB positive electrode composites. They offer electronic conductivity while simultaneously addressing interface stability and mitigating charge transport limitations, without inducing parasitic reactions with high-voltage positive electrode materials.[33,34] Recent advances demonstrate that mixed ionic-electronic conducting PEDOT variants can effectively replace conventional carbon additives and insulating binders while maintaining high active material loading (70–80 wt.%), thereby establishing a new paradigm for carbon-free solid-state battery design[32,35,36].

In this regard, the water-soluble mixed ionic-electronic polymer poly(3,4-ethylenedioxythiophene): poly(4-styrenesulfonyl(trifluoromethylsulfonyl)imide) (PEDOT:PSSTFSI), shown in Figure S1, was studied before as replacement of both binder and conductive additive in Li-ion batteries.[37] Furthermore, it‘s shown that PEDOT:PSSTFSI help to promote the formation of a thinner and more stable CEI layer compared to the PVDF:CB mixture system, particularly at higher cut-off voltages during prolonged cycling of Li-ion batteries using $LiFe_{0.4}Mn_{0.6}PO_4$ CAM system.[38] We hypothesize that the mixed conductive nature of such a functional polymer (FP) will offer significant benefit in PEC of ASSBs, acting as a multifunctional additive, i.e., as binder, electron-conductive additive, as well as ionic-conductor together with inorganic SE.

A prominent SE is lithium indium chloride, Li_3InCl_6 (LIC), which exhibits adequate ionic conductivity up to 4 mS cm^{-1},[39] and high oxidative stability up to 4.3 V vs. Li^+/Li,[40] which ensures compatibility with high-voltage CAMs.[41] Additionally, LIC can be synthesized and processed through environmentally friendly water-based methods, facilitating scalable production.[42,43] The homologous electronically conductive polymer PEDOT:PSS has already been successfully integrated into ASSBs' PEC alongside LIC, where it contributed to enhance discharge capacity of ASSBs by increasing the partial electronic conductivity of PEC.[16,30] However, PEDOT:PSS did not contribute to ionic conductivity and only a limited loading of conductive polymer was explored. This study laid the foundation of the potential using mixed ionic-electronic conductive additives to optimize PECs.

Herein, we develop a multifunctional catholyte made of Li_3InCl_6 and PEDOT:PSSTFSI, synthesized *via* facile water-mediated one-pot route. This approach allows the Li_3InCl_6 crystal particles to grow within the polymer matrix of mixed ionic-electronic conductive PEDOT:PSSTFSI, resulting in multifunctional catholyte LIC|FPX (X stands for wt.% of added FP to LIC formed). Such a configuration is designed to provide synergistic ionic-electronic transport pathways while simultaneously offering mechanical cohesion within the PEC. Thanks to the wide electrochemical stability window of PEDOT:PSSTFSI – reported to remain stable above 5 V vs Li^+/Li with signs of no overoxidation up to 6 V vs Li^+/Li [37] – this multifunctional polymer can be reliably integrated with 'single-crystalline' $LiNi_{0.6}Mn_{0.2}Co_{0.2}O_2$ (NMC622, here NMC) as the CAM, in the PEC. Thus, the LIC|FP framework is expected to enhance electronic and ionic conductivities as well as improve the mechanical compaction thanks to the polymer's soft and malleable properties. The conceptual design of this multifunctional catholyte LIC|FPX is illustrated in Schematic 1.

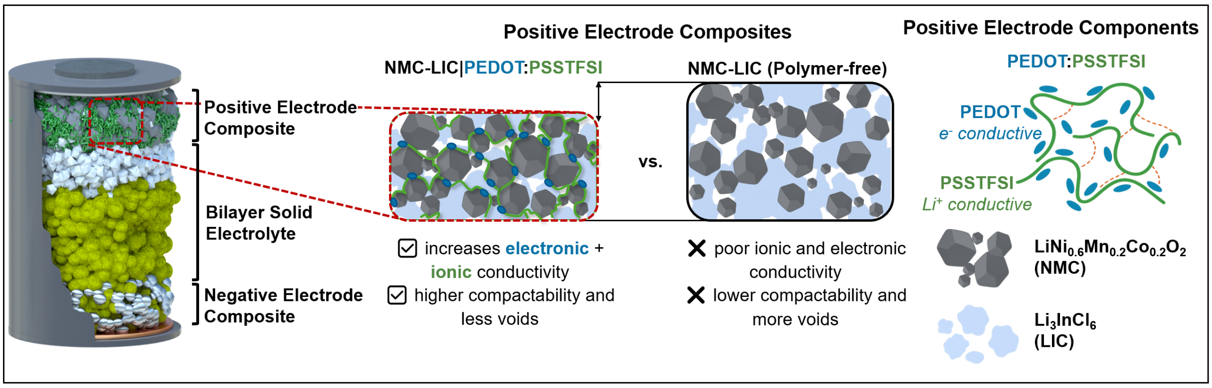

Schematic 1. Schematic of the ASSB set-up showing a PEC incorporating the multifunctional LIC|FPX (NMC-LIC|PEDOT:PSSTFSI) catholyte versus a polymer-free PEC (NMC-LIC). The use of FP enhances electrode compactness and establishes more efficient ionic and electronic conduction networks.

2. Results and Discussions

2.1. Catholyte Synthesis and Properties

A schematic illustration of the one-pot catholyte processing route of LIC with PEDOT:PSSTFSI as functional polymer (FP) is shown in Figure S2. The water-mediated synthesis represents a facile procedure conducted in water as abundant, non-toxic, and non-flammable solvent. The *in situ* aqueous synthesis route was selected to preserve the high ionic conductivity of water-synthesized LIC,[42] and the electronic conductivity of FP,[37] which are both known to be affected by additional processing. The preparation approach was optimized through trial-and-error experimental work, supported by literature.[30,42] A two-step dehydration protocol proved to be the most successful for catholyte formation. In the first step, the aqueous precursor mixture was heated at 120°C to evaporate water and concentrate the formed solid phase, while the second step at 200°C removed the residual crystalline water from $Li_3InCl_6\cdot xH_2O$ and PEDOT:PSSTFSI·xH_2O. Unlike previous reports, the evaporation temperature in the first step was increased up to 120°C to compensate for the larger total water content introduced by the aqueous FP dispersion, ensuring efficient solvent removal and homogeneous dispersion of FP within LIC precursors as well as in the formed catholyte.

Following this method, a series of catholytes, denoted as LIC|FPX, was prepared by adding LIC precursor into varying amounts of aqueous FP dispersion, enabling *in situ* synthesis of LIC within the polymer matrix. The FP was added in ratios ranging from 1 to 20 wt.% (defined by X in LIC|FPX) relative to the total mass of LIC expected to form from the reaction between LiCl and $InCl_3$. Table S1 compiles the list of notations used throughout this work to refer to the composition and formulation of the different catholytes. The corresponding recalculated FP contents in the resulting catholytes are presented in Table S2.

Figure 1a shows XRD patterns, measured with Cu K_α radiation source (λ=1.5406 Å), of the synthesized catholytes LIC|FPX. The peak reflections assigned to the main phase of Li_3InCl_6 are present for all compositions of catholyte. Their positions correspond to the monoclinic polymorph of Li_3InCl_6 described in the C2/m space group with the highest intensity reflections at 14.7°, 34.3° and 49.3°. The elevated background in the range of 10-30° corresponds to the footprint of the amorphous FP in the catholyte as supported by the XRD pattern of FP subjected to the same processing path as the catholytes (Figure S3).

The success of this processing path is also supported by the absence of the hydrated $Li_3InCl_6 \cdot xH_2O$ phase in all the studied catholyte compositions, which typically can be identified by reflections at 13.6°, 18.3°, and 31.5°.[44–46] This indicates that the removal of crystalline water after the second annealing under vacuum at 200°C was efficient, and yielded to the formation of LIC|FPX catholytes. Nevertheless, a closer inspection of the XRD patterns revealed the presence of minor unassigned reflections in catholytes with FP content from 2% at 15.6°, 17.6° and 19.4°, which became more pronounced with increasing FP content. These minor reflections do not originate from the FP, as confirmed by the XRD pattern of the PEDOT:PSSTFSI powder (Figure S3), which shows no additional reflections attributable to new crystalline phases.

To investigate the origin of these reflections, a comprehensive side-phase screening was performed, based on earlier reports on common by-products formed during water-mediated synthesis of Li_3InCl_6.[44,47] As shown in Figure S4, there is no evidence of the presence of unreacted precursors or secondary side-phases. In particular, no characteristic peak reflections were found for $InCl_3$, which is both a precursor and the product of $Li_3InCl_6 \cdot xH_2O$ decomposition. Besides, the presence of other most frequently reported side-products, such as In_2O_3, InOCl, and other metal hydroxides and oxychlorides were also excluded based on the position of peak reflections on the XRD pattern.

Another hypothesis is that the additional reflections may arise from lattice distortion of Li_3InCl_6, earlier reported for solvent-mediated synthesis of Li_3InCl_6.[48] The layered structure of Li_3InCl_6 exhibits a certain degree of structural flexibility, which facilitates formation of point defects and appearance of stacking faults supported by small energetic difference between faulted and ideal crystallographic structures.[49,50] A recent computational work[50] demonstrated that mis-staking in the [010] direction of Li_3InCl_6 lattice between $[LiCl_2]_n$ layers by 0.5 unit cell along both the a- and c- axes directions is most energetically favorable with decrease of crystal energy by 31.070 meV per formula unit compared to the ideal stacking, resulting in stable Li_3InCl_6 structure with that type of defect. The simulated XRD pattern of Li_3InCl_6 with such stacking-faults reproduces the previously unassigned peak reflections in the catholyte XRD patterns, supporting the coexistence of both ideal and distorted Li_3InCl_6 crystallographic domains. This indicates that the addition of the FP in the synthesis medium might promote lattice disorder in Li_3InCl_6, with formation of stacking faults. Importantly, such structural defects have been previously reported to enhance Li^+ conduction and being beneficial for electrochemical stability of SE.[50]

Thus, XRD analysis confirms the successful formation of Li_3InCl_6 within FP matrix in all synthesized LIC|FPX catholytes, with minor reflections that could be attributed to probable stacking disorder that does not compromise purity, overall validating the effectiveness of the one-pot synthesis approach.

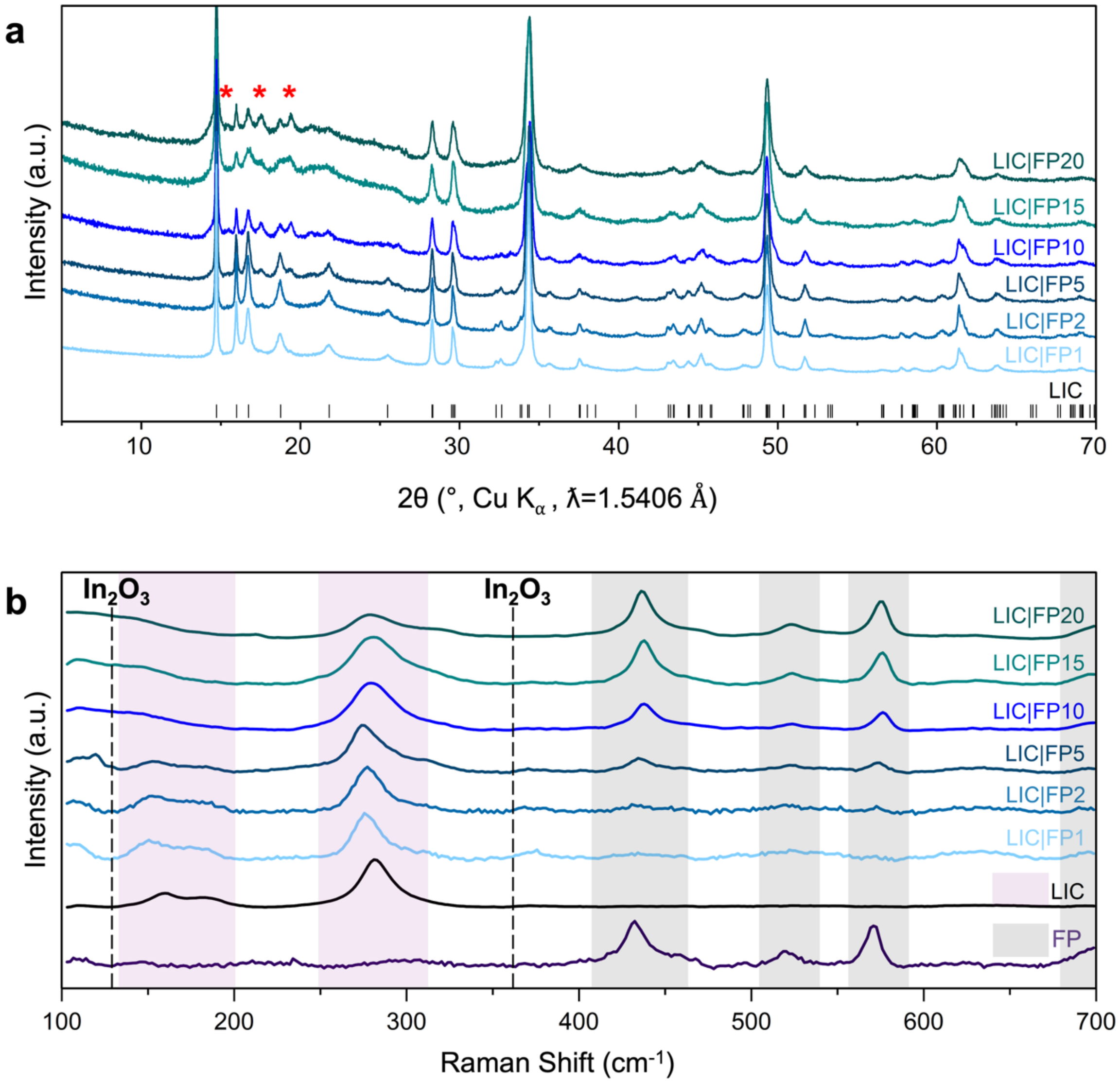

Figure 1. a) XRD patterns of the LIC|FPX catholytes, obtained with different wt.% of the FP, compared with the positions of diffraction peak reflections for LIC, as a reference. **b)** Raman spectra of the LIC|FPX catholytes along with those of the individual components, LIC and FP. The shaded regions in purple and gray correspond to the characteristic bands of LIC and FP, respectively, while the dashed line marks, if present, the expected Raman feature attributed to In_2O_3 impurities.

As shown in Figure 1b, Raman spectroscopy confirmed the presence of Li_3InCl_6 and PEDOT:PSSTFSI in the catholytes. The spectrum of pure LIC shows characteristic vibration modes at 159 and 184 cm^{-1}, with a prominent peak around 280 cm^{-1}, which is in a good agreement with previous reports on Li_3InCl_6.[47,51] Several characteristic Raman bands of Li_3InCl_6, highlighted in purple in Figure 1b, are retained in the catholytes after processing, indicating the presence of the halide electrolyte in the catholyte. At higher FP contents (LIC|FP10, LIC|FP15, and LIC|FP20), the relative intensity of the peaks at low-frequency modes at 159 and 184 cm^{-1} become significantly attenuated, which is in line with the XRD results suggesting increased structural disorder of the LIC.[47] Overall, Raman results confirm the successful incorporation of FP into the catholyte and reflects the expected compositional trend. Importantly, all spectra show no evidence of peaks at 133 and 366 cm$^{−1}$ characteristic for In_2O_3,[52] a common side-product in water-mediated LIC synthesis known to reduce ionic conductivity. [47,51] These Raman results further support the XRD findings, which shows no reflections attributable to In_2O_3 (Figure S4).

Furthermore, the addition of the PEDOT:PSSTFSI in the catholyte adds several distinct features to the spectra for the studied catholytes. In particular, peaks appear at 438, 524, 576, and 697 cm$^{−1}$, as highlighted in grey in Figure 1b, which can be attributed to various vibrational modes in PEDOT:PSSTFSI by analogy to those reported for PEDOT:PSS.[53–55] The prominent peaks at 438 cm$^{−1}$ and at 576 cm$^{−1}$ correspond to the sulfonyl group bending in PSS and oxyethylene ring deformation in PEDOT structures, the main fingerprint of PEDOT:PSS. The relative intensity of the peaks associated with FP increases with increasing FP content in the catholyte LIC|FPX, while the intensity of the peaks attributed to LIC decreases. This confirms the successful incorporation of FP into the catholyte and reflects the expected compositional trend.

Recent report suggests that the absence of crystallinity and nanostructured order in polymer binders facilitates ionic transport by creating a more connected inorganic network, thereby enhancing Li^+ conduction.[56] To confirm the nature of FP, Differential Scanning Calorimetry (DSC) measurement was performed on all studied LIC|FPX catholyte compositions to identify potential thermal phase transitions within the temperature range used for catholyte synthesis and operation. As shown in Figures S5a-d, no thermal transitions were observed for compositions containing up to 10 wt.% FP. However, glass transition temperatures (T_g) around 107–109°C were detected in samples with 15 wt.% and 20 wt.% of FP (Figures S5e-f), matching the T_g of pure FP (Figure S6). The absence of melting/crystallization peaks across all tested compositions indicates that FP remains amorphous after catholyte processing, which is consistent with the DSC results of the pure FP (Figure S6) as well as with the XRD results (Figure S3) which reveal no additional reflection which could be attributed to any crystalline phase of FP as previously discussed. Since ASSB with catholytes are typically operating at 25 °C, the FP within the catholyte remain amorphous during operation without undergoing thermal transitions in these temperature ranges.

SEM images of the LIC|FPX catholytes are presented in Figure S7. They show that the Li_3InCl_6 particles across all compositions maintain similar particle sizes, which are also comparable with the commercial Li_3InCl_6 (Figure S8). EDX mappings of powder samples (Figure S9) show a homogenous distribution of LIC within the catholyte.

2.2. Positive Electrode Composite (PEC) Preparation and Characterization

The PEC, herein noted as NMC-LIC|FPX, was prepared by homogenizing single-crystalline NMC with catholyte under mild conditions in a frequency ball mill (15 Hz for 15 min). The composition of the PEC for series with m(CAM):m(Catholyte) = 70:30 wt.%, both in wt.% and vol.% (calculated based on components' densities compiled in Table S3), are presented in Table S4, which includes the corresponding amount of FP in resulting PECs.

This deliberately mild milling protocol was chosen to solely ensure homogeneous mixing and minimize operator-dependent variability in electrode preparation, not to induce mechanochemical reactions.[57–60] Previous studies demonstrate that carefully optimized PEC preparation preserves the original microstructure of the catholyte, and X-ray diffraction (XRD) analysis of representative NMC-LIC|FP10 milled PEC confirms this: the obtained pattern (Figure S10) shows only reflections corresponding to NMC and Li_3InCl_6, with no additional peaks or shifts in existing reflections, confirming that no new crystalline phases or chemical reactions occurred during milling. These mild conditions align with established protocols for analogous systems, where no reactivity or phase transformation has been observed.[57,59,60] Thus, the ball-milling step preserved the chemical integrity of both active material and catholyte while reducing experimental uncertainty inherent in manual mixing procedures, earlier reported as frequent for higher dispersity of measurements.[30,61]

The SEM images confirm comparable morphology with similar particle sizes across all PEC compositions with ratio of m(CAM):m(Catholyte) of 70:30 wt.%: NMC-LIC|FPX (Figures 2a-c and Figure S11) with different loadings of PEDOT:PSSTFSI and NMC-LIC as reference (see Figure S12). These findings highlight the effectiveness and suitability of processing the PEC in a frequency ball-mill. Controlling the particle size is critical, as earlier studies have highlighted a significant impact of catholyte microstructure on electrochemical performance of ASSB cells.[60] By ensuring similar microstructural characteristics across all PEC, an accurate assessment of influence of FP addition on partial conductivities and cycling performance of ASSB can be performed.

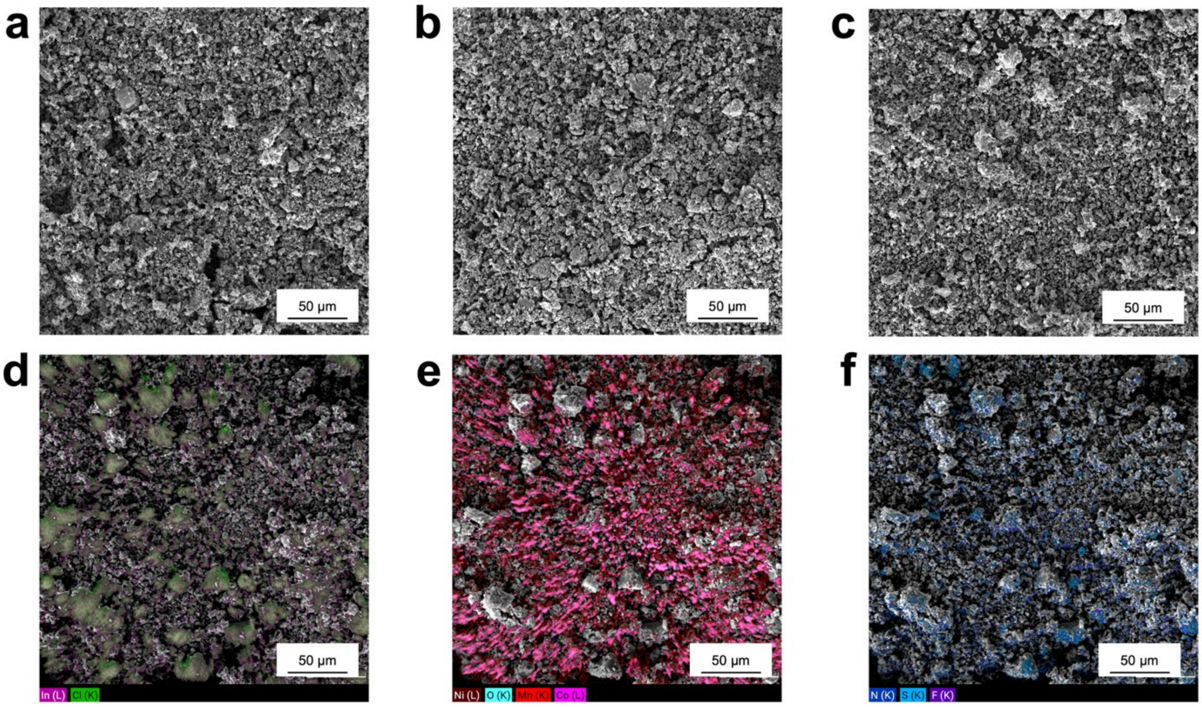

Figure 2. SEM images of PECs: **a)** NMC-LIC|FP1, **b)** NMC-LIC|FP2, and **c)** NMC-LIC|FP10. Corresponding EDX mappings of the PEC NMC-LIC|FP10 (given in c) showing distributions of elements **d)** In and Cl, **e)** Ni, O, Mn, and Co, and **f)** N, S, and F, which correspond to the main constituting compounds LIC, NMC622, and PEDOT:PSSTFSI.

Additionally, EDX mapping was conducted to evaluate the distribution of NMC, Li_3InCl_6, and PEDOT:PSSTFSI, in the PEC. Figures 2d-f and Figure S13 show that elements – Ni, Mn, Co, O, In, Cl, N, S, F – attributed to the constituent compounds of the PEC, are uniformly distributed, indicating effective homogenization between NMC (identified by Ni, Mn, Co, and O signals), LIC (In and Cl signals), and PEDOT:PSSTFSI (N, S, and F signals). These results indicate that PEC processing in a frequency ball-mill offers enhanced control over the manual grinding process, yielding uniform dispersion and only minor variation in catholyte particle sizes (Figure S7). Such homogeneous distribution of the polymer is expected to be advantageous for forming more compact PEC microstructures by improving particle-particle contact and promoting densification upon compression.[37]

To deduce how effectively FP acts as a binder, the porosity of the PEC was therefore examined prior to the electrochemical tests to assess the impact of FP incorporation on packing density and overall compactness of PECs. As shown in Figure 3, the porosity of the pellets pressed from PEC, NMC-LIC|FPX, decreases with increasing PEDOT:PSSTFSI content. The results of the theoretical density calculations accounting for the volume of FP in the PECs and exemplary measurement data for the porosity calculation are represented in Tables S5 and S6. The reference sample without FP exhibits a porosity of 42.5% which steadily decreases with the addition of FP to around 24.7% for NMC-LIC|FP20, which corresponds to only 5 wt.% FP in PEC.

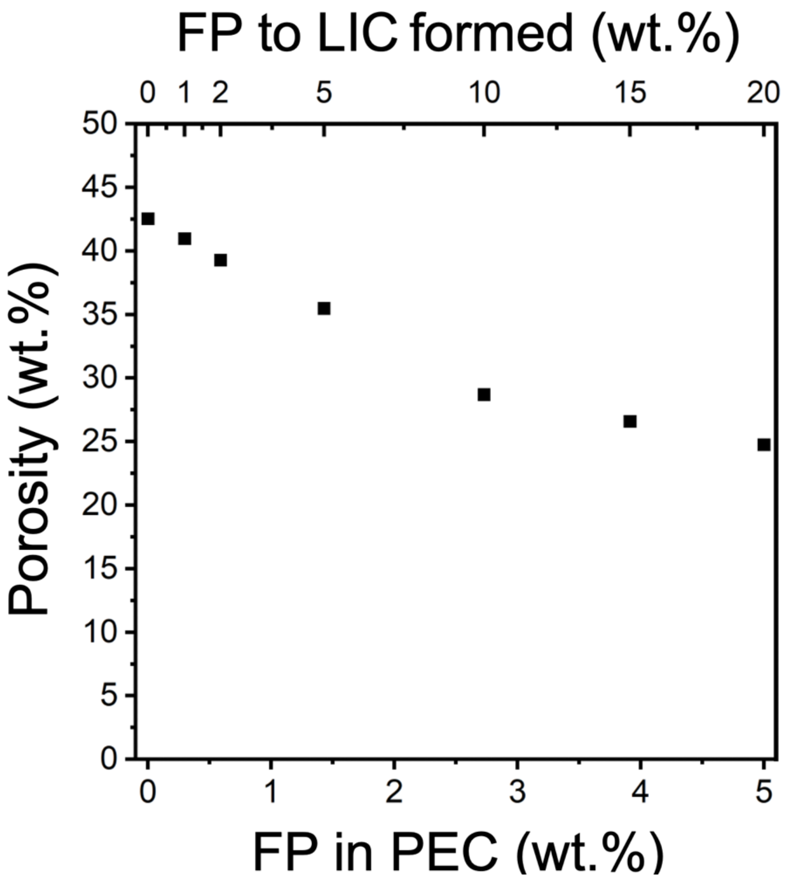

Figure 3. NMC-LIC|FPX PECs porosity as a function of FP content in the PECs with a ratio of m(CAM):m(Catholyte) = 70:30 wt.%. The porosity values were calculated from measured and theoretical densities derived from systematic density measurements summarized in Table S6 (Porosity test: measured and calculated densities for PECs).

Thus, the incorporation of FP into PEC results in a 41.9% decrease in porosity of the pellet for NMC-LIC|FP20 compared to FP-free NMC-LIC under identical processing conditions. Even small amounts of FP substantially reduce porosity, with values falling in the lower range reported for ASSB positive electrodes (20-40%).[62–65] This arises from FP's mechanical compliance: while its Young's modulus of 5.8 GPa (measured by nanoindentation using AFM)[37] matches or slightly exceeds PEDOT:PSS (2.3-5.8 GPa)[66–68] for superior stability and crack-free pellets (Figure S14), FP remains much softer and more malleable than rigid NMC622 (140 GPa)[69,70] and Li_3InCl_6 (38 GPa)[71] particles. Consequently, FP deforms preferentially during pressing, flowing into voids yielding denser electrodes.

Importantly, lower porosity implies fewer voids, better mechanical integrity of the electrode and larger contact area between active material and catholyte.[65,72,73] Consequently, Li^+ and electron transport within PEC is improved, thereby enhancing long-term cycling stability and overall battery performance, as demonstrated later in this work. Densification is particularly relevant at higher CAM loadings, where ion percolation is more challenging.[65,72,74] Notably, a porosity of below 30% at CAM loading above 55 vol.% assures the most optimal transport.[73] However, extensive densification accompanied by significant reduced porosity can disrupt the catholyte network, hindering ionic transport due to loss of a continuous ion-percolating pathways. Therefore, when a binder is used, an additional functionality contributing to transport properties is essential to optimize balanced properties.[65] Hence, a mixed ionic-electronic conducting polymer like PEDOT:PSSTFSI represents a promising material not only to effectively bind the system but also to provide a percolating network with optimized transport properties.

Similarly, catholytes LIC|FP1 and LIC|FP10 were used to prepare PECs with a ratio of m(CAM):m(Catholyte) of 80:20 wt.% (denoted as 80NMC-20LIC|FPX). The contents of all constituents both in wt.% and vol.% in PECs are shown in Table S7, while theoretical densities used for porosity calculation are given in Table S8, and the measurement results are shown in Table S9. As shown in Figure S15, the previously observed trend is maintained, *i.e.*, incorporation of FP further compacts the PEC compared to the reference. With the addition of 1.8 wt.% FP to the PEC, the porosity decreases from 36.3% for FP-free PEC to 30.8% for 80NMC-20LIC|FP10, corresponding to a relative reduction of 15.2%. However, the compactability of higher CAM PECs is less pronounced, likely due to their already compact microstructure from CAM which limits further densification through the binder.

2.3. Partial Electronic and Ionic Conductivity

In PECs which consist of the CAM and the catholyte, both electronic and ionic percolation networks are established and co-exist throughout the PEC. Such dual percolation is crucial for battery performance, as efficient electron transport enables redox reactions within the CAM, while ionic network supports Li^+ transport through the catholyte to balance the charge during (de)lithiation and sustain continuous operation. Thus, to distinguish between these two contributions and quantitatively assess the individual transport properties, which is essential to elucidate dual role of PEDOT:PSSTFSI, we performed measurements designed to separately determine the effective ionic and electronic conductivities. Using the same PECs as in porosity measurements, conductivity measurements were performed using two complementary techniques:

direct-current (DC) polarization experiments,[63] and analysis of alternating current (AC) response from electrochemical impedance spectroscopy (EIS) using a transmission line model (TLM).[72,75] To distinguish between electronic and ionic conductivities, we used symmetric cell configurations of ASSB cell casing[14] (Figure S16). To determine effective partial electronic conductivity, σ_{el}, an ion-blocking cell set-up (Figure 4a) was used, while for effective partial ionic conductivity, σ_{ion}, an electron-blocking cell set-up was used (Figure 4b). These selected cell configurations enable selective suppression of one type of charge carrier, allowing for independent evaluation.

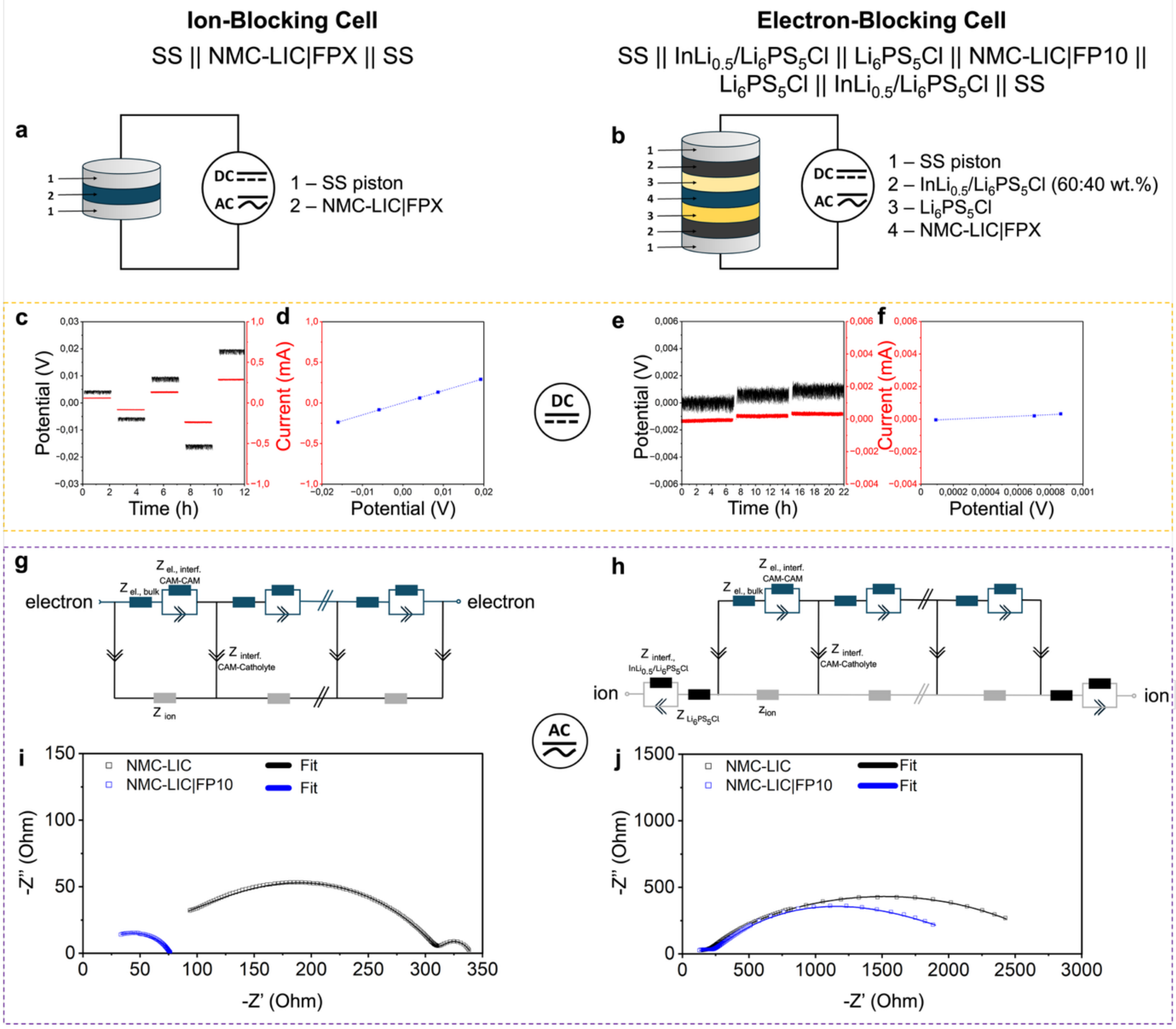

Figure 4. Cell set-ups used for partial electronic and ionic conductivity determination, and selected results of measurements performed using **DC** and **AC** methods on the representative PEC NMC-LIC|FP10 (containing 2.7 wt.% FP with m(CAM):m(Catholyte) = 70:30 wt.%). a) Ion-blocking symmetric cell for partial electronic conductivity, and b) electron-blocking symmetric

cell for partial ionic conductivity measurements. **DC method**: c), e) – current responses (red) under different applied potentials (black); d), f) – linear fits of the equilibrated current versus applied potential, measured in the ion-blocking cell setup (for c) and d)), and the electron-blocking cell setup (for e) and f)). **AC method**: interpretation of impedance measurements using the transmission line model (TLM) together with EIS data and corresponding fits for the representative PECs, NMC-LIC|FP10 compared to the polymer-free NMC-LIC. T-type transmission line model (schematically illustrated) used to fit the impedance spectra: g) ion-blocking TLM, and h) electron-blocking TLM. Impedance spectra of NMC-LIC|FP10 and polymer-free NMC-LIC, together with the corresponding TLM fits; measured data are shown as solid symbols, and the fitted curves as solid lines for i) ion-blocking and j) electron-blocking configurations.

To determine partial electronic conductivity, the PECs were pressed into pellets directly inside solid-state-battery casing in an ion-blocking cell configuration (Figure 4a). The electronic conductivity was firstly evaluated by DC polarization, with the resistance determined from the linear fit of the current-voltage response according to Ohm's law.[76] For this, a series of small DC potentials (U) was applied stepwise 2h across the symmetric cell, and the corresponding current response (I) was recorded over time, as shown on an exemplary cell containing NMC-LIC|FP10 PEC (Figure 4c). At the beginning of each step, the measured current reflects both ionic and electronic contributions. Over time, the ionic current decays due to ion-blocking electrodes, and the steady-state current (I_{ss}) corresponds mainly to electronic conduction. Hence, by plotting U (x-axis) versus I_{ss} (y-axis), a linear relation can be obtained according to Ohm's law with a slope equal to 1/R (Figure 4d). From this plot, a respective partial effective conductivity can be calculated as:

$$\sigma = \frac{L}{R \cdot A} = slope \cdot \frac{L}{A} \qquad \text{(Equation 1)}$$

Where L is the electrode thickness and A is the electrode area.

Representative current responses to the applied voltages, along with their corresponding linear fits for the entire series of studied PECs NMC-LIC and NMC-LIC|FPX, are shown in Figure S17 and Figure S18.

For the determination of partial ionic conductivity, symmetric electron-blocking cell configurations (Figure 4b) were assembled using a Li_6PS_5Cl argyrodite solid electrolyte separator and

$InLi_{0.5}/Li_6PS_5Cl$ (60:40 wt.% ratio) composite 'negative' electrodes on both sides of the 'positive' electrode composite.[63] The $InLi_{0.5}/Li_6PS_5Cl$ (60:40 wt.% ratio) 'negative electrode' is known for its stable potential and low reactivity towards sulfide electrolytes, while Li_6PS_5Cl provides ionic conductivity with improved interfacial contact.[77,78] Being in the In-InLi two phase region, here In-$(InLi)_x$ with x≈0.3 (corresponding to a Li ratio of 33.33 at.%), is crucial to ensure a stable redox potential (~ 0.622 V vs. Li^+/Li) and to enable reversible Li insertion/de-insertion, thereby avoiding degradation which typically occurs with higher Li contents in the In-Li alloys.[79] The partial ionic conductivity was calculated similarly to the procedure used for partial electronic conductivity. Representative current responses to the applied voltages, along with their corresponding linear fit for selected PEC NMC-LIC|FP10 are shown in Figure 4e-f correspondingly. Similarly, Figure S19 and Figure S20 compile the results from exemplary cells for entire series of studied PECs NMC-LIC and NMC-LIC|FPX.

The electronic and ionic conductivity values obtained by DC polarization were corroborated by AC impedance measurements using T-type transmission line model (TLM): Figure 4g – for an ion-blocking, and Figure 4h – for an electron-blocking one cell configurations. For this analysis, ion-blocking symmetric cells were modeled to extract electronic conductivity, while electron-blocking symmetric cells were used to determine ionic conductivity. The choice of the T-line model is consistent with previous reports, and a detailed description is provided in the SI.[72,75] Representative spectra and corresponding fits are shown in Figure 4i and Figure S21 (electronic conductivity, ion-blocking setup) and Figure 4j and Figure S22 (ionic conductivity, electron-blocking setup).

The resulting effective conductivities measured both with AC (stars) and DC (squares) are presented in Figure 5. The partial conductivities values are the average of at least two independent measurements to ensure reproducibility. The values obtained by AC follow the same trend as those determined by DC polarization, which confirms the reliability of both the techniques and results.

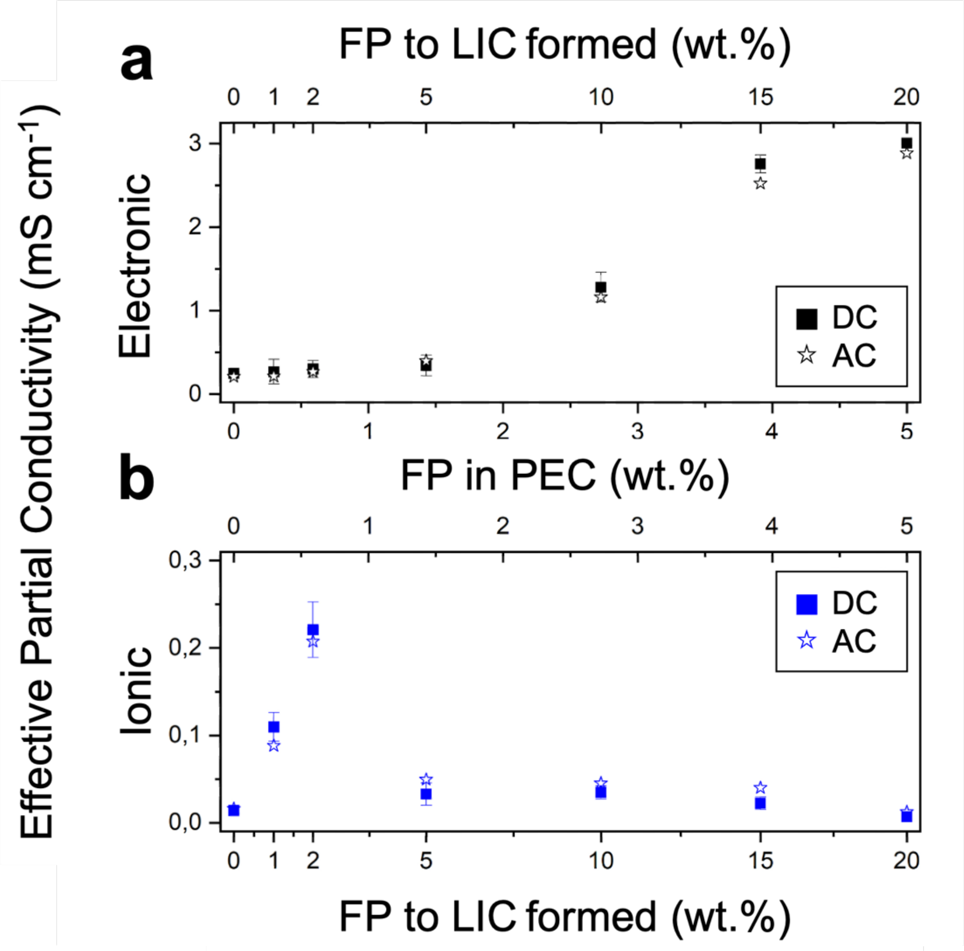

Figure 5. Effective partial conductivities: a) electronic and b) ionic, determined *via* AC (stars) and DC methods (squares).

As expected, the effective partial electronic conductivity increases with the FP content in the PEC (Figure 5a). When increasing the FP content from 1 wt.% to 20 wt.% added to the formed LIC, corresponding to 0.3 wt.% to 5 wt.% in the PEC, it results in a twelvefold increase in conductivity compared to the reference sample without any FP. This enhancement is attributed to the electronic conductivity from the extended *π*-conjugation and *π*–*π* stacking interactions within the PEDOT backbone in the multifunctional catholyte LIC|FPX (as evidenced by the respective footprints on Raman spectra, Figure 1b), which promotes more efficient electron transport throughout the PEC.

As shown in Figure 5b, the partial ionic conductivity globally increases with the addition of FP. The partial ionic conductivity reaches a maximum of 0.22 mS cm^{-1} for PEC with 0.59 wt.% FP (NMC-LIC|FP2), compared to only 0.014 mS cm^{-1} for the FP-free NMC-LIC reference, which translates to almost 16-fold increase. This result is particularly noteworthy, as it contrasts with earlier reports on PEDOT:PSS, where its incorporation in similar system reduced ionic transport due to the insulating nature of the polystyrene sulfonate, PSS in PEDOT:PSSTFSI, chains.[30] Unlike PSS, PSSTFSI acts as a single-ion conductor thanks to the TFSI$^-$ group, which facilitates better ion mobility within the PEC, thereby enhancing the overall partial ionic conductivity. Nonetheless, the effective partial ionic conductivity of the PEC first increases with the addition of PEDOT:PSSTFSI, peaking at approx. 0.6 wt.% of FP in the PEC, and begins to decrease with further increases of PEDOT:PSSTFSI.

This behavior can be attributed to the multi-functional role of PEDOT:PSSTFSI within the PEC, *i.e.*, binding, ionic, and electronic conductor. At low concentrations (up to 0.6 wt.% in PEC), the FP may enhance ionic transport by improving the interfacial contact between active materials and the SE, potentially facilitating better percolation of the ionic network. However, at higher FP contents, a gradual decrease in ionic conductivity is observed. Even though this behavior is not directly linked to the increase in partial electronic conductivity. It can instead be attributed to microstructural effects associated with the higher polymer fraction. PEDOT:PSSTFSI is intrinsically more electrically conducting than ionically conducting ($\sigma_{electrical}$=135.8 S cm^{-1}, σ_{ion}= 3.4·10^{-2} mS cm^{-1}),[37] which with further addition of FP in the PEC, can lead to a reduction in the effective volume of the ionically conducting phase, especially with volume of ionically-conducting LIC (σ_{ion}= 1.4 mS cm^{-1})[30] steadily decreasing as well (Table S4) and, consequently, to disruption of continuous ionic pathways by lowering the connectivity of ionically-conductive domains.[65,72,73]

Interestingly, this trend aligns with the evolution of the ratio between effective electronic and ionic conductivities of PEC. Figure S23 shows that for the samples based on catholytes containing 0.3 and 0.6 wt.% of FP in PECs, the ratio of $\sigma_{eff.\ el.}/\sigma_{eff.\ ion.}$ is closest to 1, indicating a balanced transport where neither ionic nor electronic transport is limiting. As highlighted in the previous work, optimal performance in ASSBs is typically achieved when the partial conductivities are in the same order of magnitude.[76] Ideally, in the case of $\sigma_{eff.\ el.}/\sigma_{eff.\ ion.} = 1$ both electrons and ions can propagate more uniformly within the PEC as Li$^+$ extraction/insertion and electron transfer occur simultaneously. Therefore, matched transport rate of Li$^+$ ion and electron is essential for uniform reaction-front propagation. When electronic conductivity exceeds ionic conductivity, Li$^+$ transport becomes limiting, causing concentration gradients and incomplete (de)lithiation; conversely, excessive ionic conductivity creates electronic bottlenecks and high overpotentials.[60,72,80,81] Consequently, in the PECs with more than 0.6 wt.% of

FP content, where electronic conductivity increases significantly, ionic mobility becomes limited which correlates with the obtained results.

Similarly, partial electronic and ionic conductivities were determined with DC and AC methods for 80NMC-20LIC|FPX PECs (composition stated in Table S7). As per DC method, representative current responses to the applied voltages, along with their corresponding linear fits for selected series of PECs 80NMC-20LIC|FPX (where X is 1 and 10), are shown in Figure S24 in ion-blocking set-ups, and Figure S25 in electron-blocking set-ups. Following the AC method, corresponding impedance spectra with their respective fits with TLM model (from Figures 4g-h) are shown in Figure S26. The resulting effective conductivities measured both with AC (stars) and DC (squares) and the ratio of $\sigma_{eff.\ el.}/\sigma_{eff.\ ion.}$ are presented in Figure S27.

In contrast to the PECs with m(CAM):m(Catholyte) = 70:30 wt.%, the addition of FP to the 80:20 wt.% system results in a slight decrease in electronic conductivity, with comparable values observed at 0.2 and 1.8 wt.% FP. Nevertheless, the overall electronic conductivity remains significantly higher than in the 70:30 wt.% PECs, both for FP-free LIC-NMC reference and PECs with a comparable ratio of FP. This can be attributed to the larger fraction of the intrinsically electron-conductive NMC particles. In parallel, the effective ionic conductivity increases upon FP addition compared to FP-free reference, highlighting the multi-functional role of the binder in promoting Li^+ transport while maintaining adequate electronic pathways.

2.4. Electrochemical Performance

2.4.1. Long Cycling Performance

In this electrochemical performance study, two PEC compositions, 1% and 10% FP, were selected as representative examples for an in-depth evaluation. As previously described, the LIC|FP1 catholyte formed a LIC phase without identifiable stacking-faults and a balanced ratio between electronic and ionic conductivities, which is essential for efficient charge transport within the PEC. In contrast, NMC-LIC|FP10 was chosen to investigate the influence of higher electronic conductivity and to evaluate the effect of increased FP content on overall electrochemical behavior. The electrochemical performance for the intermediate compositions (NMC-LIC|FP2 and NMC-LIC|FP5) are presented in the Figure S28 to provide additional comparison. Meanwhile, PEC with higher FP content (NMC-LIC|FP15 and NMC-LIC|FP20) were not further evaluated electrochemically due to the appearance of the PEDOT:PSSTFSI glass transition (T_g) in the DSC analysis, suggesting possible phase segregation or polymer chain mobility at these concentrations, as well as a significantly unbalanced electronic-to-ionic conductivity ratio that could compromise stable electrochemical performance.

The NMC-LIC|FPX were integrated into ASSB cells to investigate the impact of incorporation of the FP binder on electrochemical performance. Table S4 compiles detailed information about wt.% and vol.% of the PEC constituents for m(CAM):m(Catholyte) = 70:30 wt.%.

A bilayer SE separator (as illustrated in Schematic 1), consisting of Li_3InCl_6 and Li_6PS_5Cl, was chosen to respect the electrochemical stability windows of Li_6PS_5Cl (reduction at 1.71 V vs. Li^+/Li; oxidation at 2.01 V Li^+/Li)[82] and Li_3InCl_6 (reduction at 2.38 V vs. Li^+/Li; oxidation at 4.3 V vs. Li^+/Li).[40] This configuration was selected to mitigate the well-known chemical instability of halide-based SE in direct contact with Li metal, but also to suppress the interfacial degradation reactions leading to the growth of interfacial impedance during cycling.[57,83] Thus, to promote more stable and efficient electrochemical performance the following set-up was used NMC-LIC|FPX || Li_3InCl_6 | Li_6PS_5Cl || $InLi_{0.5}/Li_6PS_5Cl$.

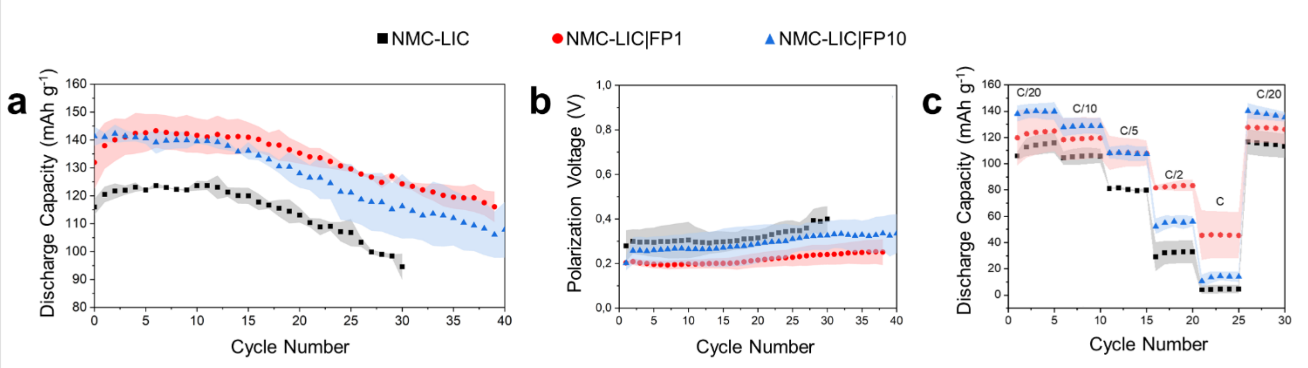

Figure 6. Electrochemical performance of PECs with varying FP contents in NMC-LIC|FPX at m(CAM):m(Catholyte) = 70:30 wt.%. a) Long-term cycling at C/20, and b) polarization voltage calculated from the cycling data. c) Rate capability testing at different C-rates. Both (a) and (c) show discharge capacities of NMC-LIC|FPX PECs with varying FP contents. The shaded regions indicate the standard deviation calculated from multiple independently measured cells.

The assembled cells were cycled within a voltage range of 2.1-3.6 V vs. $Li^+/In\text{-}InLi$ at different C rates under a constant stack pressure of 100 MPa to thoroughly evaluate the influence of incorporated PEDOT:PSSTFSI on the electrochemical performance of the ASSB. Slow rate (C/20) cycling was performed until each cell reached 80% capacity retention (CR) or reaching a maximum of 40 cycles (see Figure S28a). As shown in the Figure 6a and Figure S28b, all studied NMC-LIC|FPX compositions exhibited a higher initial discharge capacity, reaching approximately 130-145 mAh g^{-1} (NMC-LIC|FP10), compared to the FP-free NMC-LIC reference which delivered only 115-120 mAh g^{-1}. The charge - discharge curves presented in Figure S29 reveal that all NMC-LIC|FPX exhibit similar electrochemical behavior to the NMC-LIC reference, suggesting that the PEDOT:PSSTFSI does not alter the voltage characteristics or show any reactivity towards CAM or LIC. Notably, the PEDOT:PSSTFSI enhances cyclability, as seen by the increased number of cycles required for the CR to fall below 80%. In particular, the cells with FP retained 80% capacity around 40 cycles, while the NMC-LIC reference already reached this limit after 30 cycles. Further, a slight increase in discharge capacity was observed during the few initial cycles for all samples studied, which may be attributed to interface formation and stabilization processes. As shown in Figure 6a, NMC-LIC|FP1 and NMC-LIC|FP10 exhibit the most promising electrochemical performance among the tested formulations (Figure S28b), delivering the highest discharge capacities together with the longest cycle life until reaching 80% capacity retention.

To further evaluate the impact of the FP on cell behavior, the polarization voltage was quantified as the difference between the average charge ($U_{\text{average, charge}}$) and discharge ($U_{\text{average, discharge}}$) voltages of each cycle, which was used to calculate the overpotential (ΔV, calculated as $\Delta V = U_{\text{average, charge}} - U_{\text{average, discharge}}$).[61] The calculated polarization voltages are shown in Figure 6b and Figure S28c. As seen, the FP-free NMC-LIC reference exhibits the highest polarization, starting around 0.3 V and gradually increasing toward 0.45 V after 30 cycles. In contrast, all FP-containing PECs display lower polarization voltages, suggesting that PEDOT:PSSTFSI improves interfacial charge-transfer and ionic percolation within the catholyte. Among them, NMC-LIC|FP1 and NMC-LIC|FP5 achieve the lowest overall polarization (0.17-0.22 V). The NMC-LIC|FP10 PEC shows slightly higher polarization (0.25-0.30 V) than NMC-LIC|FP1 and NMC-LIC|FP5 but still significantly lower than the FP-free reference. EIS after specific charging cycles (Figure S30) confirms this trend: the polymer-free NMC-LIC reference (Figure S30c) exhibits significantly higher total resistance throughout the cycles than NMC-LIC|FP1 (Figure S30a) and NMC-LIC|FP10 (Figure S30b), which is consistent with the observed increase in polarization (Figure 6b). The slightly higher polarization observed for NMC-LIC|FP10 compared to lower FP contents may arise from an imbalance in transport pathways: while the higher FP content substantially increases the electronic conductivity of the PEC, which results in higher initial discharge capacity during long-term cycling (Figure 6a), its ionic conductivity does not increase proportionally (compared Figure 5). As a result, ionic and electronic transport are no longer optimally balanced, leading to an increase in polarization.

Overall, the reduced polarization voltage correlates directly with the improved cycling performance observed for cells assembled with FP-containing PECs. Even small additions of the polymer (0.30-1.43 wt.% in NMC-LIC|FP1 – NMC-LIC|FP5) are sufficient to lower the overpotential and enable stable long-term cycling, underscoring the multifunctional role of FP being a mixed-conductor along with effective binder. This reduction in polarization suggests that PEDOT:PSSTFSI not only enhances charge transport but also improves interfacial and mechanical integrity within the catholyte due to improved compactness of positive electrode. As a soft and malleable material, it promotes better interparticle contact by filling local voids under constant stack pressure. At the same time, the FP forms a continuous electronic network while facilitating Li^+ transport at polymer-electrolyte interfaces, supporting balanced ion-electron conduction at optimal loadings. Together, these effects lead to systematically lower overpotentials and contribute to the improved electrochemical performance observed compared to FP-free reference.

2.4.2. Rate Capability Test

To further evaluate the electrochemical performance of NMC-LIC|FP1 and NMC-LIC|FP10 (with 0.3 wt.% and 2.7 wt.% FP) under practical operating conditions, rate capability tests were performed at various C-rates. This assessment provides insights into the ability of the PEC to retain capacity at increasing charge/discharge rates, which is critical for high-power and fast-charging applications. C-rate testing often reveals limitations in ionic and electronic transport, as well as structural integrity under dynamic operating conditions. Therefore, C-rate performance could serve as a comprehensive indicator of electrochemical reliability. As shown in Figure 6c the addition of PEDOT:PSSTFSI consistently improved the discharge capacity of the NMC-LIC|FPX across all tested C-rates. The charge-discharge curve (see Figure S31) also shows a similar electrochemical profile between NMC-LIC|FPX and the FP-free NMC-LIC reference, indicating no reactivity at higher current density. The results at low C-rate show that the addition of the FP, which significantly enhances the electronic conductivity of the PEC, leads to improved performance compared to the FP-free NMC-LIC reference. Furthermore, all systems show great reversibility when the C-rate is returned to C/20 after several cycles at high current densities up to 1C, recovering most of their initial discharge capacity (ca. 125 mAh g^{-1} for NMC-LIC|FP1 and 140 mAh g^{-1} for NMC-LIC|FP10). This behavior indicates that the electrodes do not undergo significant structural degradation or irreversible side reactions during fast cycling. Whereas the observed capacity losses at high rates are likely due to transport limitation and polarization rather than permanent material damage, the observed reversibility could be associated with stable electrode/electrolyte interfaces and uniform redox processes within the CAM, both of which are critical for long-term cycling stability.[84]

As the FP content increases, the electronic conductivity within the PEC rises, indicating more efficient Li^+ extraction from the CAM compared to the FP-free sample, with NMC-LIC|FP10 outperforming other compositions at low C-rate. However, as the C-rate increases, the importance of ionic conductivity rises, since ionic transport becomes the dominant limitation to rate capability.[85] Consequently, the high-rate capability reflects the balance between electronic and ionic transport. Cells with NMC-LIC|FP1 have more comparable partial electronic and ionic conductivities and therefore outperform other tested compositions. The more balanced ionic and electronic transport are in the PEC, the better is the high-rate cycling performance. In that way efficient and uniform movement of both ions and electrons ensure that electrochemical reactions can proceed throughout the electrode more homogeneously.[76] This overall enhancement is attributed to the improved electronic and ionic conductivity provided by the mixed ionic-electronic conductive nature of PEDOT:PSSTFSI.

2.4.3. Electrochemical Cycling with Increased CAM Loading

One of the key challenges in current ASSBs lies in the high fraction of SE, required in PECs. While the SE is essential to establish continuous Li^+ pathways in ASSBs, unlike in liquid electrolyte-based lithium-ion batteries where electrolyte percolating pores ensure ionic transport, the large volume of SE reduces the proportion of CAM. This decreases the cell's overall energy density by limiting the active material and increasing the weight of inactive components. To address this issue, the CAM content in the PEC was increased, and the effect of incorporating PEDOT:PSSTFSI on electrochemical performance was evaluated. PECs with a CAM content of 80 wt.% (defined as 80NMC-20LIC|FPX) were prepared following the same procedure as for the 70 wt.% PECs, with adjustments made only to the relative proportions of CAM and catholyte.

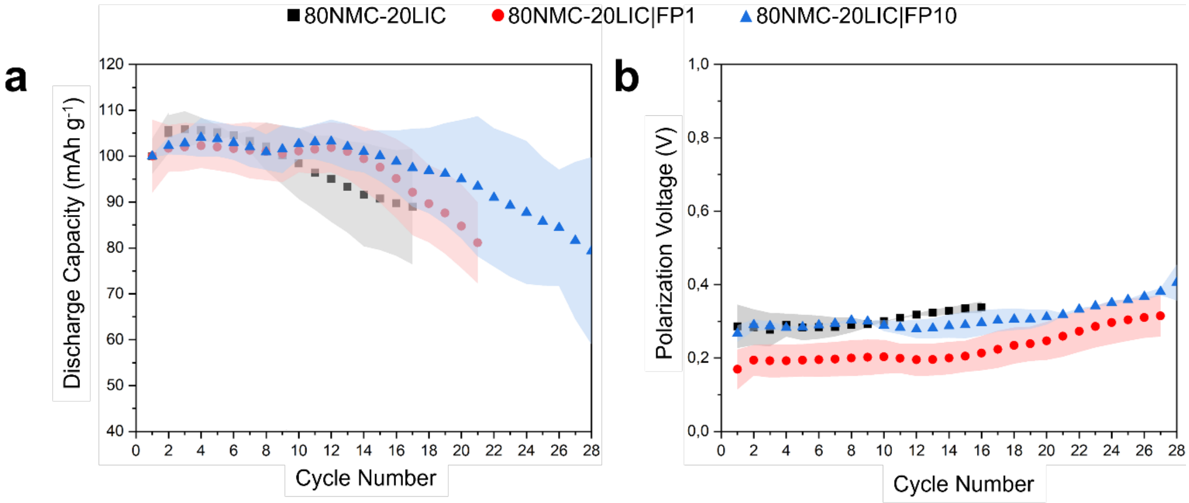

Figure 7. Electrochemical performance of PECs with varying FP contents in NMC-LIC|FPX at m(CAM):m(Catholyte) = 80:20 wt.%: a) Cycling at C/20, and b) polarization voltage calculated from the cycling data.

As shown in Figure 7a, the initial discharge capacity of the PEC with 80 wt.% CAM is slightly lower than what is obtained for the 70 wt.% CAM (compared Figure 6a). This may result from the reduced catholyte content, which limits the network for ionic percolation, as the ionically conducting phase is partially diluted by the higher NMC content. Figure S27b reveals a significant decrease in partial ionic conductivity (almost four-fold) relative to PECs with 70:30 wt.% m(CAM):m(Catholyte). Specifically for LIC|FP1 catholyte-based PECs, the ionic conductivity drops from 0.11 mS cm^{-1} (70:30 wt.% m(CAM):m(Catholyte)) to 0.03 mS cm^{-1} (80:20 wt.% m(CAM):m(Catholyte)). It should be noted, however, that the FP content differs slightly in the PEC between the two formulations (0.3 wt.% and 0.2 wt.% respectively). This difference in ionic conductivity highlights quantitatively the poor ionic network formation necessary for effective lithiation/delithiation of local CAM particles and consequently, results in poorer charge transport within the PEC.[86] The partial electronic conductivity estimated for 80:20 wt.% m(CAM):m(Catholyte) (Figure S27a) PEC exceeded that of 70:30 wt.% m(CAM):m(Catholyte) by approx. two-fold. In this case, the higher electronic conductivity originates from the increased fraction of the electronically conductive NMC in the PEC, at increased CAM loadings, the intrinsic conductivity of NMC dominates the overall electronic transport and outweighs the contribution from the polymer. Specifically for LIC|FP1 catholyte-based PECs, the electronic conductivity increases from 0.27 mS cm^{-1} (70:30 wt.% m(CAM):m(Catholyte)) to 0.48 mS cm^{-1} (80:20 wt.% m(CAM):m(Catholyte)). As shown in Figure S27c, the ratio $\sigma_{eff.\ el.}/\sigma_{eff.\ ion.}$ is thus significantly larger (e.g., 8.5 for 80NMC-20LIC|FP1) than in the PECs with 70:30 wt.% m(CAM):m(Catholyte) (e.g., 2.4 for NMC-LIC|FP1), indicating a pronounced imbalance between electronic and ionic transport. This demonstrates that, while the 80NMC-20LIC|FPX PEC provides sufficient electronic pathways to extract Li^+ from the NMC particles, its markedly lower ionic conductivity severely limits ion mobility within the positive electrode, thereby hindering uniform (de)lithiation of the active material and reducing overall electrochemical utilization.

The polarization voltage for 80:20 PEC systems was calculated identically to 70:30 PEC systems. Figure 7b reveals consistent trend: 80NMC-20LIC|FP1 achieves the lowest initial polarization (0.17 V) but exhibits accelerated degradation, increasing to 0.31 V over 27 cycles ($\Delta V = 0.14$ V) – substantially steeper than 70NMC-30LIC|FP1 ($\Delta V = 0.03$ V over 27 cycles). The FP-free 80NMC-20LIC reference exhibits the highest polarization, reaching 0.34 V after only 16 cycles (corresponding to 80% capacity retention). Meanwhile, 80NMC-20LIC|FP10 PECs exhibit comparable polarization to 80NMC-20LIC reference, with a rather continuous increase ($\Delta V = 0.14$ V) over the 28 cycles (corresponding to 80% capacity retention).

Notwithstanding polarization comparable to 80NMC-20LIC FP-free reference, the incorporation of PEDOT:PSSTFSI significantly enhanced the cyclability of the 80NMC-20LIC|FP10 PEC, maintaining stable performance up to 28 cycles (see Figure S32 for charge-discharge results) before reaching 80% capacity retention. This improvement can be ascribed to PEDOT:PSSTFSI binding properties improving compactness of PEC (as seen in Figure S15), in addition to the mixed electronic and ionic conductive nature, which facilitates better interparticle contact compared to FP-free NMC-LIC reference.

3. Conclusion and Outlook

In this study, we successfully demonstrated a one-pot synthesis approach for incorporating functional polymer (FP) PEDOT:PSSTFSI in Li_3InCl_6 (LIC) solid electrolyte, and systematically investigated its effects on mechanical integrity, electronic and ionic conductivity, and overall electrochemical performance. X-ray diffraction and Raman spectroscopy confirmed the formation of a high-purity LIC phase with PEDOT:PSSTFSI that retained its functionality. Scanning electronic microscopy suggested the formation of LIC in the polymer network, with homogeneous distribution of FP in positive electrode composite (PEC) with $LiNi_{0.6}Mn_{0.2}Co_{0.2}O_2$ (NMC). Thanks to its soft and malleable nature, the incorporation of PEDOT:PSSTFSI improved the compactness of the PEC pellets, reducing the residual porosity, which is advantageous for long-term cycling stability.

Additionally, the mixed conductive nature of PEDOT:PSSTFSI significantly enhanced both partial electronic and ionic conductivity within the PEC, contributing to improved electrochemical performance. Long-term cycling results showed that the PEC with PEDOT:PSSTFSI achieved higher discharge capacity with a greater number of cycles before reaching 80% capacity retention compared to FP-free reference, NMC-LIC. Further, the incorporation of the PEDOT:PSSTFSI not only enhances partial electronic and ionic conductivity but also rate performance and capacity recovery after high-rate cycling rates, underscoring its potential for stable, high-rate performance. While direct comparison with other ASSB systems remains challenging due to variations in bilayer SE stacks, composite negative electrode configurations, and testing protocols across reported works, the systematic optimization of FP content presented here provides a valuable benchmark for future development of multifunctional polymer-inorganic composites, outscoring previous reports of using PEDOT:PSS in ASSB with similar setups.[30,33]

Lastly, the incorporation of PEDOT:PSSTFSI enables increasing the CAM content in the PEC formulation up to 80 wt.% while maintaining stable cyclability. Overall, PEDOT:PSSTFSI serves as a multifunctional additive, acting as a binder, electronic conductor, and ionic conductor within this PEC system, making it a promising component for scalable ASSB. Future work may focus on reducing the cell stack pressure during cycling. In this study, we demonstrated that incorporating PEDOT:PSSTFSI increases the density of PEC pellets, which may enable operation at lower stack pressures. Furthermore, exploration of LIC formation in various solvents and/or optimizing PEDOT:PSSTFSI synthesis in different media could further improve LIC yield and conductivity, as solvent choice significantly affects the polymer’s structural and electrical properties.[39] Additionally, extending application of multifunctional catholytes to other cathode active material (CAM) chemistries, such as NMC with higher Ni-content, represents a promising direction leveraging PEDOT:PSSTFSI’s proven stability above 5 V vs. Li^+/Li.

A fundamental study aimed at understanding how PEDOT:PSSTFSI influences ionic and electronic transport, using advanced techniques such as 3D tomography, tortuosity analysis or modeling would provide valuable insights into the polymer’s role in enhancing ion/electron pathways, composite densification, and stress distribution within the electrode. Meanwhile, post-mortem analysis such as cross-sectional morphology imaging and XPS, are critical to elucidate Li_3InCl_6 distribution evolution, interfacial layer chemistry, and mechanistic degradation pathways during extended cycling. Such studies would directly correlate interfacial morphology with long-term electrochemical stability, clarifying how PEDOT:PSSTFSI's mechanical and transport properties mitigate stress-induced phenomena at composite's boundaries.

4. Experimental Section

4.1. Materials

PSSTFSIK as previously synthesized by Nugraha, et al.,[37] 3,4-ethylenedioxythiophene (EDOT, TCI, >98%), $(NH_4)_2S_2O_8$ 98% (Sigma Aldrich), anhydrous $FeCl_3$ (Sigma Aldrich), lithium chloride (LiCl, Sigma Aldrich, 99%), indium chloride anhydrous ($InCl_3$, Sigma Aldrich, 99.99%), NMC ($LiNi_{0.6}Mn_{0.2}Co_{0.2}O_2$, monolithic, MSE Supplies), lithium indium chloride (Li_3InCl_6, NEI Corporation), lithium phosphorus sulfur chloride, i.e., sulfide argyrodite (Li_6PS_5Cl, NEI Corporation), lithium (Li, 99.9%), indium foil (In, 99.999%, Sigma Aldrich).

4.2. Methods

Synthesis of Mixed Ionic-Electronic Conductive Polymer PEDOT:PSSTFSI. The PEDOT:PSSTFSI complex, whose chemical structure is shown in Figure S1, was synthesized by classical oxidative polymerization of 3,4-Ethylenedioxythiophene (EDOT) in the aqueous solution of the obtained PSSTFSI in deionized (DI) water with the ratio of EDOT:SSTFSI being 0.5 using $(NH_4)_2S_2O_8$ and $FeCl_3$ oxidants with ratio of 3.5 and oxidant:EDOT of 2.3.[37] After 72 h at 10 °C, the polymer dispersions were purified using Lewatit S100 KR/H and Lewatit MP62WS ion exchange resins (60 mg of resin per 1 mL of PEDOT:PSSTFSI aqueous dispersion). The solution was then concentrated using an ultrafiltration cell with 100 kDa ultrafiltration discs (Amicon bioseparations). The concentration of the PEDOT:PSSTFSI aqueous dispersion was determined by measuring its absorbance in a 1 mm optical glass cell with a UV-360 Shimadzu UV-Vis-NIR-Spectrophotometer. The relation between the absorbance and the concentration was determined previously using the Beer-Lambert law: $C = 0.565 \times Abs.$[87]

One-Pot Synthesis of Li_3InCl_6-PEDOT:PSSTFSI Catholyte. The process steps are illustrated schematically in Figure S2. Dry LiCl and $InCl_3$ precursors were weighed in a 3:1 molar ratio and homogenized in an agate mortar with pestle in the Ar-filled glovebox. This mixture was then solubilized in an 8 mL vial with DI water (150-1000 µL depending on the batch size) under air and mixed with the weighed amount of PEDOT:PSSTFSI aqueous dispersion in accordance with its concentration and the amount of the expected Li_3InCl_6. The added amounts of PEDOT:PSSTFSI investigated in this study were 1, 2, 5, 10, 15, and 20 % of the total amount of the expected Li_3InCl_6 to-be-formed. After dissolution, water was removed by heating on a hot plate and in a heating block at 120 °C until no visible water remained. The color of the obtained dry powder varied from light grey to dark blue depending on the added amount of PEDOT:PSSTFSI. It was then quickly ground before being transferred to a vacuum *Buchi* oven and annealed in two 4 h steps at 200 C with intermediate hand-grinding in the Ar-filled glovebox. After thermal processing and prior to use, the synthesized catholyte – consisting of LIC and PEDOT:PSSTFSI in different concentrations – was hand-ground for 5 min in the agate mortar to loosen up and to homogenize particles. The obtained product was named LIC|FPX, with X being equal to 1, 2, 5, 10, 15, or 20 %, corresponding to the wt.% of added PEDOT:PSSTFSI to LIC to-be-formed. The used nomenclature to refer to the compounds is compiled in Table S1. The recalculated wt.% of FP in LIC|FPX catholyte, based on the amount of FP added to LIC precursors, is presented in Table S2 of the SI.

Characterization of Li_3InCl_6-PEDOT:PSSTFSI Catholyte. X-ray diffraction (XRD) experiments were carried out with a X’Pert3 diffractometer equipped with a capillary spinner and a Cu K_α X-ray source, λ=1.5406 Å). The catholyte was packed into a 0.3 mm diameter borosilicate glass capillary inside of Ar-filled glovebox. The measurements were conducted over an angular range of 5-70° (2θ) with a step size of 0.017° and time per step 550s.

Differential scanning calorimetry (DSC) measurements were performed in aluminum pans (sealed hermetically inside Ar-filled glovebox) using a DSC Q250 (TA Instruments) with a heating rate of 10 °K min^{-1} in a temperature range between 25 °C – 250 °C for at least 2 heating/cooling cycles. The results were analyzed with TRIOS software.

Catholyte samples were subjected to Raman spectroscopy analysis. It was performed on samples densely packed into a 0.3 mm diameter borosilicate glass capillary. A confocal LabRAM HR Evolution micro-spectrometer equipped with a laser with wavelength of 532 nm was used for the measurements, the laser power, laser attenuation (filtering), time and number of acquisitions were adjusted sample to sample to provide adequate quality of signal. The spectra were recorded in the Raman shift range of 100-700 cm^{-1} with a spectral resolution of 3-5 cm^{-1}. The acquired data were processed using Horiba LabSpec 6 software.

Preparation of Positive Electrode Composite (PEC) The PEC of NMC-LIC|FPX was prepared using the mini-mill PULVERISETTE 23 (Fritsch) with 5 mL ball mill cup. Inside the Ar-filled glovebox, the weighted quantities of NMC and LIC|FPX in different weight ratios m(CAM):m(Catholyte) of 70:30 and 80:20, were transferred into a small ball mill cup together with 5 mm ZrO_2 grinding balls. The mixture was then gently milled at 15 Hz for 15 min. By this way, PECs noted as NMC-LIC|FPX for each combination of m(CAM):m(Catholyte) were obtained. Densities of the constituents (compiled in Table S3) were used to estimate the densities of PECs with different m(CAM):m(Catholyte) ratios: Table S5 (for 70:30 wt.%) and Table S8 (for 80:20 wt.%). The composition of PECs with different m(CAM):m(Catholyte) both in wt.% and vol.% are summarized in Table S4 (for 70:30 wt.%) and Table S7 (for 80:20 wt.%).

SEM-EDX analysis was conducted to investigate the morphology of the synthesized catholytes and PECs. It was performed using a TESCAN Vega microscope equipped with a tungsten electron source and operated at an accelerating voltage of 15 kV and a beam current of 30-40 pA for SEM imaging and 3-4 nA for EDX. The samples were prepared as follows: the powder was dispersed onto carbon tape mounted on SEM stubs, and the excess was gently tapped off. The samples were then sputter-coated with gold inside Ar-filled glovebox. After sputtering, the samples on the stubs were transferred from glovebox to the SEM using an air-tight container. From the container, the samples were promptly mounted on the SEM with minimal exposure to atmosphere air. The images and EDX were processed on TESCAN Essence Software.

The porosity of the PEC was accessed to determine the impact of PEDOT:PSSTFSI addition on packing density and compactness of PECs. Therefore, to access the porosity of the PEC, the geometrical approach was used to estimate the density, based on the average thickness, mass loading and geometrical shape. For this, approx. 50 mg of PEC powder was pressed into a pellet using 8 mm diameter press-die at a pressure of 4 t cm^{-2} for 5 min. After pressing and extraction of the pellet from the press-die, the thickness of the pellet and pellet mass were measured. These values were used to calculate the measured density, ρ_{meas}, of the pellet. Subsequently, porosity was determined as follows:

$$\text{Porosity} = \left(1 - \frac{\rho_{meas}}{\rho_{theo}}\right) \cdot 100\%.$$

The theoretical density of the PEC with polymer additive, ρ_{theo}, was calculated based on the densities of the individual constituents, weighted by their respective mass fractions in the composites.

$$\rho_{theo} = \frac{1}{\frac{w_{\mathrm{CAM}}}{\rho_{\mathrm{CAM}}} + \frac{w_{\mathrm{SE}}}{\rho_{\mathrm{SE}}} + \frac{w_{\mathrm{FP}}}{\rho_{\mathrm{FP}}}}$$

Theoretical densities for NMC (4.81 g cm^{-3})[57] and LIC (2.69 g cm^{-3})[76] were derived from their crystallographic lattice parameters. The density of the PEDOT:PSSTFSI (1.88 g cm^{-3}) was determined experimentally. Specifically, the PEDOT:PSSTFSI powder, obtained from the aqueous dispersion following the processing route shown in Figure S2, was measured at room temperature using a helium pycnometer (Quantachrome UltraPycnometer 1000).

Measurements were performed over 100 cycles with a gas flow time of 3 minutes per cycle, and the reported density corresponds to the average value of all measurements.

Preparation of Negative Electrode Composite. The negative electrode composite, $InLi_{0.5}/Li_6PS_5Cl$ (60:40 wt.% ratio), was used in this study to assemble ASSB half-cells subjected for evaluation of electrochemical performance with addition of FP into catholyte. The anode composite was prepared *via* a two-step route following an established procedure.[14] First, a 1:2 atomic ratio Li to In was enveloped in In foil. Second, the foil was laminated and folded several times with a glass tube until the In-Li alloy became darker and brittle. Finally, the corresponding amount of Li_6PS_5Cl powder was weighed and added into a mortar, and hand-ground for 30 min together with the In-$(InLi)_x$ alloy to ensure optimum homogeneity of the $InLi_{0.5}/Li_6PS_5Cl$ anode composite.

Partial Electronic and Ionic Conductivity Measurement. Effective partial electronic conductivities of the PECs were measured in symmetric cells. Materials and cell components handling, including uniaxial powder pressing and cell assembly, was performed in Ar-filled glovebox. All measurements were performed in the ASSB press-cell (schematically represented in Figure S16) with a two-electrode cell set-up. The press cell consists of a polyetherimide (PEI) cell sleeve (8 mm diameter) and two stainless steel (SS) current collector pistons (4 mm radius, 0.5 cm^2 area).[14] Two methods were used to quantify the transport properties: direct current (DC) polarization measurements and Electrochemical Impedance Spectroscopy (EIS) with alternating current (AC). All measurements were performed at 25 °C temperature.

First, ion-blocking set-up (Figure 4a) was assembled to quantify partial effective electronic conductivity of PECs NMC-LIC|FPX with different PEDOT:PSSTFSI loadings in catholyte. For this, ca. 50 mg of PEC was weighed and transferred into the cell sleeve, which was closed on one side with a piston. After carefully spreading the PEC over the piston surface, the cell was closed with the second piston and pressed at 2 t cm^{-2} for 3 min. The pistons in this set-up serve as ion-blocking electrodes. The ASSB casing was then closed air-tight with seals and tightened with six screws to a pressure of 100 MPa (screws were tightened with a torque of 2.3 Nm in the specific cell design used in Figure S16). For the DC polarization method, a series of different potentials (from -5 mV to 20 mV) were applied stepwise till the measured current reaches equilibrium state after 2 h. To confirm the findings, an alternative AC technique was used. Potentiostatic EIS was performed with an amplitude of 10 mV in the range of frequencies from 10 mHz to 1 MHz on a BioLogic VMP3 Model Potentiostat.

Secondly, an electron-blocking set-up (Figure 4b) was used to determine partial effective ionic conductivity of NMC-LIC|FPX PECs. For this, on both sides of the 50 mg composite pressed earlier, 40 mg of Li_6PS_5Cl powder was transferred and pressed at 2 t cm^{-2} for 3 min. Finally, on each side of the pressed pellets 15 mg of the 'negative' electrode composite $InLi_{0.5}/Li_6PS_5Cl$ was placed and spread evenly. The ASSB casing was then closed air-tight with seals, pressed with 4 t cm^{-2} for 5 min and tightened with six screws to a pressure of 100 MPa (screws were tightened with a torque of 2.3 Nm). For the DC polarization method, a range of voltages from 1 to 5 mV was applied to the symmetric cell. The measured current equilibration time was increased to 7 h. Similarly, before cell polarization a potentiostatic EIS measurement was performed in the same range of frequencies as for ion-blocking cell. EIS data from potentiostat were analyzed using RelaxIS 3 software (rhd instruments GmbH & Co. KG).

Electrochemical Performance Evaluation. ASSBs cells were assembled in three steps. First, 35 mg of Li_6PS_5Cl were transferred to the cell sleeve and pressed at 2 t cm^{-2} for 2 minutes. Second, 15 mg of Li_3InCl_6 were added on top of the Li_6PS_5Cl and the bilayer stack was pressed at 2 t cm^{-2} for 2 min. Finally, positive electrode and negative electrode composites were transferred in the sleeve: $InLi_{0.5}/Li_6PS_5Cl$ (25 mg), on top of Li_6PS_5Cl and NMC-LIC|FPX (8 mg), on top of Li_3InCl_6. All powders were carefully and evenly spread after being transferred inside the cell sleeve and compacted with a SS stamp prior to pressure application to ensure homogeneity.

The full cell stack, NMC-LIC|FPX || Li_3InCl_6 | Li_6PS_5Cl || $InLi_{0.5}/Li_6PS_5Cl$, was then pressed at 4 t cm^{-2} for 5 min. The ASSB casing was then closed air-tight with seals and tightened with six screws to a pressure of 100 MPa (screws were tightened with a torque of 2.3 Nm in the specific cell design used in Figure S16). The PECs with a 70:30 wt.%, m(CAM):m(Catholyte) ratio resulted in an areal loading of 11.14 mg_{NMC} cm^{-2}. The PECs with 80:20 wt.%, m(CAM):m(Catholyte) ratio resulted in an areal loading of 12.73 mg_{NMC} cm^{-2}.

Electrochemical testing was performed at 25 °C in the potential range of 2.1–3.6 vs. Li^+/In-InLi (taking that 0 V vs. Li^+/In-InLi is ~ 0.622 V vs. Li^+/Li) with symmetrical constant current charging and discharging using two protocols: 1) long-term cycling at a C/20 rate with EIS measurement at specific cycles in the fully charge state and 2) rate capability testing at various C-rates from C/20 to 1C. A rate of 1C corresponds to the current required to theoretically exchange 1 Li^+ (or 1 electron) per formula unit within 1 h (i.e., a full charge in 1 h) with 276 mAh g^{-1} as a theoretical capacity for NMC622. The exact current density, j, is calculated as $j =$

$Areal\ loading \cdot Specific\ Capacity_{NMC} \cdot C_{rate}$. The electrochemical measurements were performed on BioLogic VMP3 Model Potentiostat. The potentiostatic EIS was performed during long-term cycling at C/20 rate. Measurements were conducted after cells rested for a minimum of 1 h to reach stable open circuit voltage following specific charge cycles. EIS spectra were acquired on a BioLogic VMP3 Model Potentiostat with an AC amplitude of 10 mV in the range of frequencies from 1 Hz to 1 MHz.

Acknowledgements

The authors gratefully acknowledge the support and funding from the European Union's Horizon 2020 research and innovation program under the Marie Skłodowska-Curie Actions (Grant Agreement No. 945357, Destiny PhD Program), the Nouvelle-Aquitaine Region (Project AAPR2021A-2020-11998810), the French National Research Agency (STORE-EX Labex Project ANR-10-LABX-76-01) and BayFrance (Franco-Bavarian University Cooperation Center). The authors would also like to extend their sincere thanks to Emmanuel Petit, Céline Sanvoisin, Olivier Nguyen, Rafael Bianchini Nuernberg and Eric Lebraud from ICMCB, and to Mélanie Bousquet and Benjamin Cabannes-Boue from LCPO, for their valuable assistance in daily experimental procedures and scientific discussions.

Data Availability Statement

The data that support the findings of this study are available in the Supporting Information.

Conflict of Interest

The authors declare no conflict of interest.

References

[1] R. Chen, Q. Li, X. Yu, L. Chen, H. Li, "Approaching Practically Accessible Solid-State Batteries: Stability Issues Related to Solid Electrolytes and Interfaces" *Chem Rev* 2020, *120*, 6820–6877.

[2] L. Li, H. Duan, J. Li, L. Zhang, Y. Deng, G. Chen, "Toward High Performance All-Solid-State Lithium Batteries with High-Voltage Cathode Materials: Design Strategies for Solid Electrolytes, Cathode Interfaces, and Composite Electrodes" *Adv Energy Mater* 2021, *11*, DOI 10.1002/aenm.202003154.

[3] N. Boaretto, I. Garbayo, S. Valiyaveettil-SobhanRaj, A. Quintela, C. Li, M. Casas-Cabanas, F. Aguesse, "Lithium solid-state batteries: State-of-the-art and challenges for materials, interfaces and processing" *J Power Sources* 2021, *502*, DOI 10.1016/j.jpowsour.2021.229919.

[4] L. (CATL) Contemporary Amperex Technology Co., “ Innovative Technology. High Energy Density Technology Exceeding Limitations.,” can be found under https://www.catl.com/en/research/technology/(accessed 18 November 2025), n.d.

[5] V. Kumaravel, J. Bartlett, S. C. Pillai, 2021, Wiley-VCH Verlag preprint, DOI: 10.1002/aenm.202002869.

[6] P. Lu, Z. Zhou, Z. Xiao, J. Lu, J. Zhang, G. Hu, W. Yan, S. Xia, S. Zhang, Z. Wang, H. Li, C. Wang, F. Wu, X. Sun, “Materials and chemistry design for low-temperature all-solid-state batteries” *Joule* 2024, *8*, 635–657.

[7] B. Hong, L. Gao, C. Li, G. Lai, J. Zhu, D. Huang, Y. Zuo, W. Yin, M. Sun, S. Zhao, J. Zheng, S. Han, R. Zou, “All-solid-state batteries designed for operation under extreme cold conditions” *Nature Communications* 2025, *16*, DOI 10.1038/s41467-024-55154-5.

[8] X. Miao, S. Guan, C. Ma, L. Li, C. W. Nan, “Role of Interfaces in Solid-State Batteries” *Advanced Materials* 2023, *35*, DOI 10.1002/adma.202206402.

[9] T. Famprikis, P. Canepa, J. A. Dawson, M. S. Islam, C. Masquelier, “Fundamentals of inorganic solid-state electrolytes for batteries” *Nat Mater* 2019, *18*, 1278–1291.

[10] H. Al-Salih, M. S. E. Houache, E. A. Baranova, Y. Abu-Lebdeh, 2022, John Wiley and Sons Inc preprint, DOI: 10.1002/aesr.202200032.

[11] P. Minnmann, F. Strauss, A. Bielefeld, R. Ruess, P. Adelhelm, S. Burkhardt, S. L. Dreyer, E. Trevisanello, H. Ehrenberg, T. Brezesinski, F. H. Richter, J. Janek, “Designing Cathodes and Cathode Active Materials for Solid-State Batteries” *Adv Energy Mater* 2022, *12*, 2201425.

[12] A. I. Pitillas Martinez, F. Aguesse, L. Otaegui, M. Schneider, A. Roters, A. Llordés, L. Buannic, “The Cathode Composition, A Key Player in the Success of Li-Metal Solid-State Batteries” *Journal of Physical Chemistry C* 2019, *123*, 3270–3278.

[13] E. Schlautmann, J. Drews, L. Ketter, M. A. Lange, T. Danner, A. Latz, W. G. Zeier, “Graded Cathode Design for Enhanced Performance of Sulfide-Based Solid-State Batteries” *ACS Energy Lett* 2025, *10*, 1664–1670.

[14] E. Quemin, R. Dugas, T. Koç, B. Hennequart, R. Chometon, J. M. Tarascon, “Decoupling Parasitic Reactions at the Positive Electrode Interfaces in Argyrodite-Based Systems” *ACS Appl Mater Interfaces* 2022, *14*, 49284–49294.

[15] W. Zhang, T. Leichtweiß, S. P. Culver, R. Koerver, D. Das, D. A. Weber, W. G. Zeier, J. Janek, “The Detrimental Effects of Carbon Additives in Li10GeP2S12-Based Solid-State Batteries” *ACS Appl Mater Interfaces* 2017, *9*, 35888–35896.

[16] C. Wang, J. Liang, J. Luo, J. Liu, X. Li, F. Zhao, R. Li, H. Huang, S. Zhao, L. Zhang, J. Wang, X. Sun, *A universal wet-chemistry synthesis of solid-state halide electrolytes for all-solid-state lithium-metal batteries*, 2021.

[17] H. seung Kim, S. Park, S. Kang, J. Y. Jung, K. S. Kim, J. S. Yu, D. W. Kim, J. W. Lee, Y. K. Sun, W. Cho, “Accelerated Degradation of All-Solid-State Batteries Induced through Volumetric Occupation of the Carbon Additive in the Solid Electrolyte Domain” *Adv Funct Mater* 2024, *34*, DOI 10.1002/adfm.202409318.

[18] Y. Bae Song, H. Kwak, W. Cho, K. S. Kim, Y. Seok Jung, K. H. Park, 2022, Elsevier Ltd preprint, DOI: 10.1016/j.cossms.2021.100977.

[19] A. De Gol, K. B. Dermenci, L. Farkas, M. Berecibar, 2024, John Wiley and Sons Inc preprint, DOI: 10.1002/aenm.202403255.

[20] X. Hu, Z. Zhang, X. Zhang, Y. Wang, X. Yang, X. Wang, M. Fayena-Greenstein, H. A. Yehezkel, S. Langford, D. Zhou, B. Li, G. Wang, D. Aurbach, 2024, Nature Research preprint, DOI: 10.1038/s41578-024-00669-y.

[21] J. M. Doux, Y. Yang, D. H. S. Tan, H. Nguyen, E. A. Wu, X. Wang, A. Banerjee, Y. S. Meng, "Pressure effects on sulfide electrolytes for all solid-state batteries" *J Mater Chem A Mater* 2020, *8*, 5049–5055.

[22] C. Mao, J. Dong, J. Li, X. Zhai, J. Ma, S. Luan, X. Shen, Y. Wang, P. Zhang, H. Sun, X. Bie, X. Gao, J. Song, 2025, John Wiley and Sons Inc preprint, DOI: 10.1002/adma.202500079.

[23] N. Stankiewicz, M. Criado-Gonzalez, J. L. Olmedo-Martínez, E. Matxinandiarena, P. López-Aranguren, F. Bonilla, G. Accardo, D. Saurel, D. Devaux, I. Villaluenga, "In Situ Hybrid Solid-State Electrolytes for Lithium Battery Applications" *ACS Appl Polym Mater* 2024, *6*, 14124–14132.

[24] H. Li, G. Du, H. Liang, Q. Su, D. Han, W. Zhao, M. Zhang, S. Ding, B. Xu, "High-capacity all-solid-state lithium battery with stable interfaces enabled by ultra-thin polyvinylidene fluoride/Li3InCl6 composite solid electrolyte" *J Alloys Compd* 2023, *969*, DOI 10.1016/j.jallcom.2023.172418.

[25] Z. Li, J. Fu, X. Zhou, S. Gui, L. Wei, H. Yang, H. Li, X. Guo, 2023, John Wiley and Sons Inc preprint, DOI: 10.1002/advs.202201718.

[26] S. Kundu, Y. Ein-Eli, "A review on design considerations in polymer and polymer composite solid-state electrolytes for solid Li batteries" *J Power Sources* 2023, *553*, DOI 10.1016/j.jpowsour.2022.232267.

[27] Z. Wan, D. Lei, W. Yang, C. Liu, K. Shi, X. Hao, L. Shen, W. Lv, B. Li, Q. H. Yang, F. Kang, Y. B. He, "Low Resistance–Integrated All-Solid-State Battery Achieved by Li7La3Zr2O12 Nanowire Upgrading Polyethylene Oxide (PEO) Composite Electrolyte and PEO Cathode Binder" *Adv Funct Mater* 2019, *29*, DOI 10.1002/adfm.201805301.

[28] G. L. Gregory, H. Gao, B. Liu, X. Gao, G. J. Rees, M. Pasta, P. G. Bruce, C. K. Williams, "Buffering Volume Change in Solid-State Battery Composite Cathodes with CO2-Derived Block Polycarbonate Ethers" *J Am Chem Soc* 2022, *144*, 17477–17486.

[29] S. Deng, M. Jiang, N. Chen, W. Li, M. Zheng, W. Chen, R. Li, H. Huang, J. Wang, C. V. Singh, X. Sun, "Regulating Electronic Conductivity at Cathode Interface for Low-Temperature Halide-Based All-Solid-State Batteries" *Adv Funct Mater* 2022, *32*, DOI 10.1002/adfm.202205594.

[30] E. Nazmutdinova, C. Rosenbach, C. Schmidt, S. Sarawutankul, K. Neuhaus, A. Gröschel, N. M. Vargas-Barbosa, "On the Influence of Li3InCl6−PEDOT:PSS Hybrids

in Solid-State Batteries Prepared via an Aqueous One-Pot Approach” *Batter Supercaps* 2024, *7*, DOI 10.1002/batt.202300434.

[31] H. Li, F. Lian, N. Meng, C. Xiong, N. Wu, B. Xu, Y. Li, “Constructing Electronic and Ionic Dual Conductive Polymeric Interface in the Cathode for High-Energy-Density Solid-State Batteries” *Adv Funct Mater* 2021, *31*, DOI 10.1002/adfm.202008487.

[32] R. del Olmo, T. C. Mendes, M. Forsyth, N. Casado, “Mixed ionic and electronic conducting binders containing PEDOT:PSS and organic ionic plastic crystals toward carbon-free solid-state battery cathodes” *J Mater Chem A Mater* 2022, *10*, 19777–19786.

[33] S. Deng, M. Jiang, N. Chen, W. Li, M. Zheng, W. Chen, R. Li, H. Huang, J. Wang, C. V. Singh, X. Sun, “Regulating Electronic Conductivity at Cathode Interface for Low-Temperature Halide-Based All-Solid-State Batteries” *Adv Funct Mater* 2022, *32*, DOI 10.1002/adfm.202205594.

[34] S. Deng, Y. Sun, X. Li, Z. Ren, J. Liang, K. Doyle-Davis, J. Liang, W. Li, M. Norouzi Banis, Q. Sun, R. Li, Y. Hu, H. Huang, L. Zhang, S. Lu, J. Luo, X. Sun, “Eliminating the Detrimental Effects of Conductive Agents in Sulfide-Based Solid-State Batteries” *ACS Energy Lett* 2020, *5*, 1243–1251.

[35] E. Nazmutdinova, C. Rosenbach, C. Schmidt, S. Sarawutankul, K. Neuhaus, A. Gröschel, N. M. Vargas-Barbosa, “On the Influence of Li3InCl6−PEDOT:PSS Hybrids in Solid-State Batteries Prepared via an Aqueous One-Pot Approach” *Batter Supercaps* 2024, *7*, DOI 10.1002/batt.202300434.

[36] L. Zhao, Q. Dong, X. Wang, Z. Li, H. Shao, Y. Shen, L. Chen, “Organic Mixed Ionic-Electronic Conductors as Multi-Functional Binders for Energy-Dense Carbon-Free Solid-State Batteries” *Batter Supercaps* 2024, *7*, DOI 10.1002/batt.202400132.

[37] I. M. Nugraha, J. Olchowka, C. Brochon, D. Flahaut, M. Bousquet, B. Cabannes-Boue, R. Bianchini Nuernberg, É. Cloutet, L. Croguennec, “An Alternative Polymer Material to PVDF Binder and Carbon Additive in Li-Ion Battery Positive Electrode” *Advanced Science* 2024, DOI 10.1002/advs.202409403.

[38] I. M. Nugraha, D. Flahaut, J. Olchowka, C. Brochon, R. Bianchini Nuernberg, É. Cloutet, L. Croguennec, “Revealing the role of functional binder PEDOT:PSSTFSI in cathode–electrolyte interphase formation on LiFe0.4Mn0.6PO4electrodes of Li-ion batteries” *J Mater Chem A Mater* 2025, DOI 10.1039/d5ta06213f.

[39] J. O. Bonsu, A. Bhadra, D. Kundu, “Wet Chemistry Route to Li3InCl6: Microstructural Control Render High Ionic Conductivity and Enhanced All-Solid-State Battery Performance” *Advanced Science* 2024, *11*, DOI 10.1002/advs.202403208.

[40] S. Wang, Q. Bai, A. M. Nolan, Y. Liu, S. Gong, Q. Sun, Y. Mo, “Lithium Chlorides and Bromides as Promising Solid-State Chemistries for Fast Ion Conductors with Good Electrochemical Stability” *Angewandte Chemie* 2019, *131*, 8123–8127.

[41] J. Shi, Y. Zhu, J. Wang, M. Khan, F. Ning, X. Liu, S. Lu, J. Yi, “High-Voltage Induced Stable Interface Promoting Electrochemical Performance for Halide-Based All-Solid-State Batteries” *ACS Appl Energy Mater* 2025, *8*, 13894–13901.

[42] X. Li, J. Liang, N. Chen, J. Luo, K. R. Adair, C. Wang, M. N. Banis, T. Sham, L. Zhang, S. Zhao, S. Lu, H. Huang, R. Li, X. Sun, “Water-Mediated Synthesis of a Superionic Halide Solid Electrolyte” *Angewandte Chemie* 2019, *58*, 16427–16432.

[43] X. Li, J. Liang, J. Luo, M. Norouzi Banis, C. Wang, W. Li, S. Deng, C. Yu, F. Zhao, Y. Hu, T. K. Sham, L. Zhang, S. Zhao, S. Lu, H. Huang, R. Li, K. R. Adair, X. Sun, “Air-stable Li3InCl6 electrolyte with high voltage compatibility for all-solid-state batteries” *Energy Environ Sci* 2019, *12*, 2665–2671.

[44] J. Y. Huang, K. Iputera, Y. T. Lin, Y. T. Hung, Y. S. Liu, Y. P. Chang, B. Bazri, B. H. Liu, D. H. Wei, B. Y. Jin, R. S. Liu, “Exploring dehydration mechanisms and conductivity optimization in Li3InCl6$xH2O via in situ synchrotron techniques” *J Mater Chem A Mater* 2024, *13*, 2895–2901.

[45] R. L. Sacci, T. H. Bennett, A. R. Drews, V. Anandan, M. J. Kirkham, L. L. Daemen, J. Nanda, “Phase evolution during lithium-indium halide superionic conductor dehydration” *J Mater Chem A Mater* 2021, *9*, 990–996.

[46] H. W. Liu, C. C. Lin, P. Y. Chang, S. C. Haw, H. S. Sheu, J. M. Chen, C. C. Chen, R. J. Jeng, N. L. Wu, “Reducing oxy-contaminations for enhanced Li-ion conductivity of halide-based solid electrolyte in water-mediated synthesis” *Journal of Solid State Electrochemistry* 2022, *26*, 2089–2096.

[47] W. Li, J. Liang, M. Li, K. R. Adair, X. Li, Y. Hu, Q. Xiao, R. Feng, R. Li, L. Zhang, S. Lu, H. Huang, S. Zhao, T. K. Sham, X. Sun, “Unraveling the origin of moisture stability of halide solid-state electrolytes by in situ and operando synchrotron X-ray analytical techniques” *Chemistry of Materials* 2020, *32*, 7019–7027.

[48] R. Xiong, L. Yuan, R. Song, S. Hao, H. Ji, Z. Cheng, Y. Zhang, B. Jiang, Y. Shao, Z. Li, Y. Huang, “Solvent-Mediated Synthesis and Characterization of Li3InCl6 Electrolytes for All-Solid-State Li-Ion Battery Applications” *ACS Applied Materials and Interfaces* 2024, *16*, 36281–36288.

[49] E. Kim, Y. Kim, “Investigation of the effect of point defects on the Li-ion conductivity of Li3InCl6” *Dalton Transactions* 2022, *51*, 18159–18168.

[50] Y. Kim, S. Choi, “Investigating stacking variations in Li3InCl6 crystal structure and their influence on solid electrolyte properties” *Acta Mater* 2024, *276*, DOI 10.1016/j.actamat.2024.120135.

[51] S. Wang, X. Xu, C. Cui, C. Zeng, J. Liang, J. Fu, R. Zhang, T. Zhai, H. Li, “Air Sensitivity and Degradation Evolution of Halide Solid State Electrolytes upon Exposure” *Adv Funct Mater* 2022, *32*, 2108805.

[52] D. Liu, W. Lei, S. Qin, L. Hou, Z. Liu, Q. Cui, Y. Chen, “Large-scale synthesis of hexagonal corundum-type In2O 3 by ball milling with enhanced lithium storage capabilities” *J Mater Chem A Mater* 2013, *1*, 5274–5278.

[53] S. Nešpůrek, P. Kuberský, R. Polanský, M. Trchová, J. Šebera, V. Sychrovský, “Raman spectroscopy and DFT calculations of PEDOT:PSS in a dipolar field” *Physical Chemistry Chemical Physics* 2022, *24*, 541–550.

[54] S. Sakamoto, M. Okumura, Z. Zhao, Y. Furukawa, “Raman spectral changes of PEDOT-PSS in polymer light-emitting diodes upon operation” *Chem Phys Lett* 2005, *412*, 395–398.

[55] M. Kong, M. Garriga, J. S. Reparaz, M. I. Alonso, “Advanced Optical Characterization of PEDOT:PSS by Combining Spectroscopic Ellipsometry and Raman Scattering” *ACS Omega* 2022, *7*, 39429–39436.

[56] N. Stankiewicz, L. Focks, M. Cui, M. Fernandez, E. Modin, A. Iturrospe, O. Pajuelo-Corral, E. Simon, A. Arbe, P. Siffalovic, G. R. Goward, A. Chuvilin, I. Villaluenga, “Unveiling the crucial morphological effect of non-conducting polymer binders on inorganic-rich hybrid electrolytes” *J Mater Chem A Mater* 2025, DOI 10.1039/d5ta00979k.

[57] C. Rosenbach, F. Walther, J. Ruhl, M. Hartmann, T. A. Hendriks, S. Ohno, J. Janek, W. G. Zeier, “Visualizing the Chemical Incompatibility of Halide and Sulfide-Based Electrolytes in Solid-State Batteries” *Adv Energy Mater* 2023, *13*, DOI 10.1002/aenm.202203673.

[58] S. Puls, L. Ketter, W. G. Zeier, N. M. Vargas-Barbosa, “Opportunities and Limitations of Partial Transport Quantification in All-Solid-State Composite Electrodes” *ACS Electrochemistry* 2025, DOI 10.1021/acselectrochem.5c00258.

[59] O. Maus, M. A. Lange, F. Frankenberg, F. Stainer, V. Faka, E. Schlautmann, C. Rosenbach, A. Jodlbauer, J. Schubert, J. Janek, C. Li, P. Michalowski, H. M. R. Wilkening, A. Kwade, W. G. Zeier, “Influence of Post-Synthesis Processing on the Structure, Transport, and Performance of the Solid Electrolyte Li5.5PS4.5Cl1.5 in All-Solid-State Batteries” *Adv Energy Mater* 2025, *15*, DOI 10.1002/aenm.202403291.

[60] E. Schlautmann, A. Weiß, O. Maus, L. Ketter, M. Rana, S. Puls, V. Nickel, C. Gabbey, C. Hartnig, A. Bielefeld, W. G. Zeier, “Impact of the Solid Electrolyte Particle Size Distribution in Sulfide-Based Solid-State Battery Composites” *Adv Energy Mater* 2023, DOI 10.1002/aenm.202302309.

[61] S. Puls, E. Nazmutdinova, F. Kalyk, H. M. Woolley, J. F. Thomsen, Z. Cheng, A. Fauchier-Magnan, A. Gautam, M. Gockeln, S. Y. Ham, M. T. Hasan, M. G. Jeong, D. Hiraoka, J. S. Kim, T. Kutsch, B. Lelotte, P. Minnmann, V. Miß, K. Motohashi, D. L. Nelson, F. Ooms, F. Piccolo, C. Plank, M. Rosner, S. E. Sandoval, E. Schlautmann, R. Schuster, D. Spencer-Jolly, Y. Sun, B. S. Vishnugopi, R. Zhang, H. Zheng, P. Adelhelm, T. Brezesinski, P. G. Bruce, M. Danzer, M. El Kazzi, H. Gasteiger, K. B. Hatzell, A. Hayashi, F. Hippauf, J. Janek, Y. S. Jung, M. T. McDowell, Y. S. Meng, P. P. Mukherjee, S. Ohno, B. Roling, A. Sakuda, J. Schwenzel, X. Sun, C. Villevieille, M. Wagemaker, W. G. Zeier, N. M. Vargas-Barbosa, “Benchmarking the reproducibility of all-solid-state battery cell performance” *Nat Energy* 2024, *9*, 1310–1320.

[62] S. Choi, M. Jeon, J. Ahn, W. D. Jung, S. M. Choi, J. S. Kim, J. Lim, Y. J. Jang, H. G. Jung, J. H. Lee, B. I. Sang, H. Kim, “Quantitative Analysis of Microstructures and Reaction Interfaces on Composite Cathodes in All-Solid-State Batteries Using a Three-Dimensional Reconstruction Technique” *ACS Appl Mater Interfaces* 2018, *10*, 23740–23747.

[63] E. Schlautmann, A. Weiß, O. Maus, L. Ketter, M. Rana, S. Puls, V. Nickel, C. Gabbey, C. Hartnig, A. Bielefeld, W. G. Zeier, “Impact of the Solid Electrolyte Particle Size Distribution in Sulfide-Based Solid-State Battery Composites” *Adv Energy Mater* 2023, DOI 10.1002/aenm.202302309.

[64] T. Shi, Y. Q. Zhang, Q. Tu, Y. Wang, M. C. Scott, G. Ceder, “Characterization of mechanical degradation in an all-solid-state battery cathode” *J Mater Chem A Mater* 2020, *8*, 17399–17404.

[65] A. Bielefeld, D. A. Weber, J. Janek, “Modeling Effective Ionic Conductivity and Binder Influence in Composite Cathodes for All-Solid-State Batteries” *ACS Appl Mater Interfaces* 2020, *12*, 12821–12833.

[66] K. Rohtlaid, G. T. M. Nguyen, C. Soyer, E. Cattan, F. Vidal, C. Plesse, “Poly(3,4-ethylenedioxythiophene):Poly(styrene sulfonate)/Polyethylene Oxide Electrodes with Improved Electrical and Electrochemical Properties for Soft Microactuators and Microsensors” *Adv Electron Mater* 2019, *5*, DOI 10.1002/aelm.201800948.

[67] D. Tank, H. H. Lee, D. Y. Khang, “Elastic moduli of organic electronic materials by the buckling method” *Macromolecules* 2009, *42*, 7079–7083.

[68] U. Lang, J. Dual, “Mechanical Properties of the Intrinsically Conductive Polymer Poly(3,4- Ethylenedioxythiophene) Poly(Styrenesulfonate) (PEDOT/PSS)” *Key Eng Mater* 2007, *345–346*, 1189–1192.

[69] X. Sun, L. Wang, J. Ma, X. Yu, S. Zhang, X. Zhou, G. Cui, “A Bifunctional Chemomechanics Strategy to Suppress Electrochemo-Mechanical Failure of Ni-Rich Cathodes for All-Solid-State Lithium Batteries” *ACS Appl Mater Interfaces* 2022, *14*, 17674–17681.

[70] I. U. Haq, S. Lee, “Molecular Dynamics Study of the Ni Content-Dependent Mechanical Properties of NMC Cathode Materials” *Crystals (Basel)* 2025, *15*, DOI 10.3390/cryst15030272.

[71] P. Molaiyan, S. E. Mailhiot, K. Voges, A. M. Kantola, T. Hu, P. Michalowski, A. Kwade, V. V. Telkki, U. Lassi, “Investigation of the structure and ionic conductivity of a Li3InCl6 modified by dry room annealing for solid-state Li-ion battery applications” *Mater Des* 2023, *227*, DOI 10.1016/j.matdes.2023.111690.

[72] P. Minnmann, L. Quillman, S. Burkhardt, F. H. Richter, J. Janek, “Editors’ Choice—Quantifying the Impact of Charge Transport Bottlenecks in Composite Cathodes of All-Solid-State Batteries” *J Electrochem Soc* 2021, *168*, 040537.

[73] A. Bielefeld, D. A. Weber, J. Janek, “Microstructural Modeling of Composite Cathodes for All-Solid-State Batteries” *Journal of Physical Chemistry C* 2019, *123*, 1626–1634.

[74] T. Shi, Q. Tu, Y. Tian, Y. Xiao, L. J. Miara, O. Kononova, G. Ceder, “High Active Material Loading in All-Solid-State Battery Electrode via Particle Size Optimization” *Adv Energy Mater* 2020, *10*, DOI 10.1002/aenm.201902881.

[75] Z. Siroma, T. Sato, T. Takeuchi, R. Nagai, A. Ota, T. Ioroi, “AC impedance analysis of ionic and electronic conductivities in electrode mixture layers for an all-solid-state lithium-ion battery” *J Power Sources* 2016, *316*, 215–223.

[76] T. Hendriks, M. Lange, E. Kiens, C. Baeumer, W. Zeier, “Balancing Partial Ionic and Electronic Transport for Optimized Cathode Utilization of High-voltage LiMn2O4 / Li3InCl6 Solid-state Batteries” *Batter Supercaps* 2023, DOI 10.1002/batt.202200544.

[77] S. Luo, Z. Wang, X. Li, X. Liu, H. Wang, W. Ma, L. Zhang, L. Zhu, X. Zhang, “Growth of lithium-indium dendrites in all-solid-state lithium-based batteries with sulfide electrolytes” *Nat Commun* 2021, *12*, DOI 10.1038/s41467-021-27311-7.

[78] W. J. Jeong, C. Wang, S. G. Yoon, Y. Liu, T. Chen, M. T. McDowell, “Electrochemical behavior of elemental alloy anodes in solid-state batteries” *ACS Energy Lett* 2024, *9*, 2554–2563.

[79] A. L. Santhosha, L. Medenbach, J. R. Buchheim, P. Adelhelm, “The Indium−Lithium Electrode in Solid-State Lithium-Ion Batteries: Phase Formation, Redox Potentials, and Interface Stability” *Batter Supercaps* 2019, *2*, 524–529.

[80] T. Hendriks, M. Lange, E. Kiens, C. Baeumer, W. Zeier, “Balancing Partial Ionic and Electronic Transport for Optimized Cathode Utilization of High-voltage LiMn2O4 / Li3InCl6 Solid-state Batteries” *Batter Supercaps* 2023, DOI 10.1002/batt.202200544.

[81] G. F. Dewald, S. Ohno, J. G. C. Hering, J. Janek, W. G. Zeier, “Analysis of Charge Carrier Transport Toward Optimized Cathode Composites for All-Solid-State Li−S Batteries” *Batter Supercaps* 2021, *4*, 183–194.

[82] Y. Zhu, X. He, Y. Mo, “Origin of Outstanding Stability in the Lithium Solid Electrolyte Materials: Insights from Thermodynamic Analyses Based on First-Principles Calculations” *ACS Appl Mater Interfaces* 2015, *7*, 23685–23693.

[83] A. Tron, A. Beutl, I. Mohammad, A. Paolella, “Insights into the chemical and electrochemical behavior of halide and sulfide electrolytes in all-solid-state batteries” *Energy Advances* 2025, *4*, 518–529.

[84] Y. Xiao, Y. Wang, S. H. Bo, J. C. Kim, L. J. Miara, G. Ceder, 2020, Nature Research preprint, DOI: 10.1038/s41578-019-0157-5.

[85] R. Tian, S. H. Park, P. J. King, G. Cunningham, J. Coelho, V. Nicolosi, J. N. Coleman, “Quantifying the factors limiting rate performance in battery electrodes” *Nat Commun* 2019, *10*, DOI 10.1038/s41467-019-09792-9.

[86] Q. S. Liu, H. W. An, X. F. Wang, F. P. Kong, Y. C. Sun, Y. X. Gong, S. F. Lou, Y. F. Shi, N. Sun, B. Deng, J. Wang, J. J. Wang, “Effective transport network driven by tortuosity gradient enables high-electrochem-active solid-state batteries” *Natl Sci Rev* 2023, *10*, DOI 10.1093/nsr/nwac272.

[87] A. Glasser, É. Cloutet, G. Hadziioannou, H. Kellay, “Tuning the Rheology of Conducting Polymer Inks for Various Deposition Processes” *Chemistry of Materials* 2019, *31*, 6936–6944.